

## ARTICLE



# The phosphorylation and dephosphorylation switch of VCP/p97 regulates the architecture of centrosome and spindle

Kaiyuan Zhu<sup>1,2,6</sup>, Yang Cai<sup>3,6</sup>, Xiaotong Si<sup>1,2,6</sup>, Zuodong Ye<sup>1,2</sup>, Yuanzhu Gao<sup>4</sup>, Chuang Liu<sup>4</sup>, Rui Wang<sup>1,2</sup>, Zhibin Ma<sup>1,2</sup>, Huazhang Zhu<sup>1,2</sup>, Liang Zhang<sup>1,2</sup>, Shengjin Li<sup>5</sup>, Hongmin Zhang<sup>3</sup> and Jianbo Yue<sup>1,2</sup>

© The Author(s), under exclusive licence to ADMC Associazione Differenziamento e Morte Cellulare 2022

The proper orientation of centrosome and spindle is essential for genome stability; however, the mechanism that governs these processes remains elusive. Here, we demonstrated that polo-like kinase 1 (Plk1), a key mitotic kinase, phosphorylates residue Thr76 in VCP/p97 (an AAA-ATPase), at the centrosome from prophase to anaphase. This phosphorylation process recruits VCP to the centrosome and in this way, it regulates centrosome orientation. VCP exhibits strong co-localization with Eg5 (a mitotic kinesin motor), at the mitotic spindle, and the dephosphorylation of Thr76 in VCP is required for the enrichment of both VCP and Eg5 at the spindle, thus ensuring proper spindle architecture and chromosome segregation. We also showed that the phosphatase, PTEN, is responsible for the dephosphorylation of Thr76 in VCP; when PTEN was knocked down, the normal spread of VCP from the centrosome to the spindle was abolished. Cryo-EM structures of VCP<sup>T76A</sup> and VCP<sup>T76E</sup>, which represent dephosphorylated and phosphorylated states of VCP, respectively, revealed that the Thr76 phosphorylation modulates VCP by altering the inter-domain and inter-subunit interactions, and ultimately the nucleotide-binding pocket conformation. Interestingly, the tumor growth in nude mice implanted with VCP<sup>T76A</sup>-reconstituted cancer cells was significantly slower when compared with those implanted with VCP<sup>WT</sup>-reconstituted cancer cells. Collectively, our findings demonstrate that the phosphorylation and dephosphorylation switch of VCP regulates the architecture of centrosome and spindle for faithful chromosome segregation.

*Cell Death & Differentiation* (2022) 29:2070–2088; <https://doi.org/10.1038/s41418-022-01000-4>**INTRODUCTION**

The centrosomes mainly acts as a microtubule-organizing center. In dividing cells, the centrosome is duplicated during the S phase, and moves to a bipolar position at M phase, thereby controlling the nucleation, assembly, and orientation of the bipolar mitotic spindle [1, 2]. The correct orientation of the bipolar mitotic spindle is essential for faithful chromosome segregation, and this process is tightly regulated by a cascade of protein phosphorylation and proteolysis events centering on the cyclin B-Cdk1 complex, the master mitotic kinase. The cyclin B-Cdk1 complex interacts with other mitotic kinases (e.g., Aurora kinases and polo-like kinase 1 (Plk1)), to precisely control the progression of the M-phase, including the orientation of the centrosome and the spindle [3, 4]. Errors in these processes can lead to mitotic catastrophe or genome instability, which are hallmarks of many diseases, including cancer [5].

Plk1 is composed of an N-terminal kinase domain and a C-terminal duplicated polo-box domain (PBD) connected by a short linker. Plk1 is activated after Aurora-A (with the help of Bora), phosphorylates a threonine residue in the activation loop of Plk1. The activated Plk1, in turn, phosphorylates a variety of substrates via its PBD to regulate M phase progression, starting from mitotic

entry, and including centrosome maturation, bipolar spindle formation, cohesin dissociation, chromosome alignment, the spindle assembly checkpoint (SAC), APC/C activation, and cytokinesis. Plk1 is enriched in the centrosomes, kinetochores, and midbody during M phase [6, 7]. Moreover, it is overexpressed in different types of tumors, and several Plk1 inhibitors are currently being tested in a number of anti-cancer clinical trials [8, 9].

Plk1 regulates centrosome separation via Eg5 (also known as kinesin-5), which is a major motor protein for centrosome movement. Eg5, a homotetramer, is widely dispersed in the cytosol during interphase and it moves toward the plus-end of the mitotic spindle during mitosis [10]. At the beginning of mitosis, Plk1 phosphorylates the NIMA-family kinases, Nek6/7, and once activated, Nek6/7 together with Cdk1 subsequently phosphorylate various sites in Eg5 to promote its accumulation at the centrosome [11–13]. Eg5 then “walks” toward the plus end of the microtubule to establish the bipolar spindle [14]. Centrosome movement is also regulated by PTEN (a dual-specificity protein and lipid phosphatase known to be involved in tumor suppression), via dephosphorylation of Eg5 at Thr926 and/or by acting as a scaffold protein [15, 16]. It has also been known that the mechanical coupling of Eg5 is enhanced by the acetylation of

<sup>1</sup>City University of Hong Kong Shenzhen Research Institute, Shenzhen, China. <sup>2</sup>Department of Biomedical Sciences, City University of Hong Kong, Hong Kong, China. <sup>3</sup>Department of Biology, Southern University of Science and Technology, Shenzhen 518055, China. <sup>4</sup>Department of Biology, SUSTech Cryo-EM Centre, Southern University of Science and Technology, Shenzhen 518055, China. <sup>5</sup>The Second Affiliated Hospital of Chongqing Medical University, Chongqing, China. <sup>6</sup>These authors contributed equally: Kaiyuan Zhu, Yang Cai, Xiaotong Si. ✉email: 300288@cqmu.edu.cn; zhanghm@sustech.edu.cn; jianbyue@cityu.edu.hk  
Edited by M. Piacentini

Received: 27 July 2021 Revised: 30 January 2022 Accepted: 28 March 2022

Published online: 16 April 2022

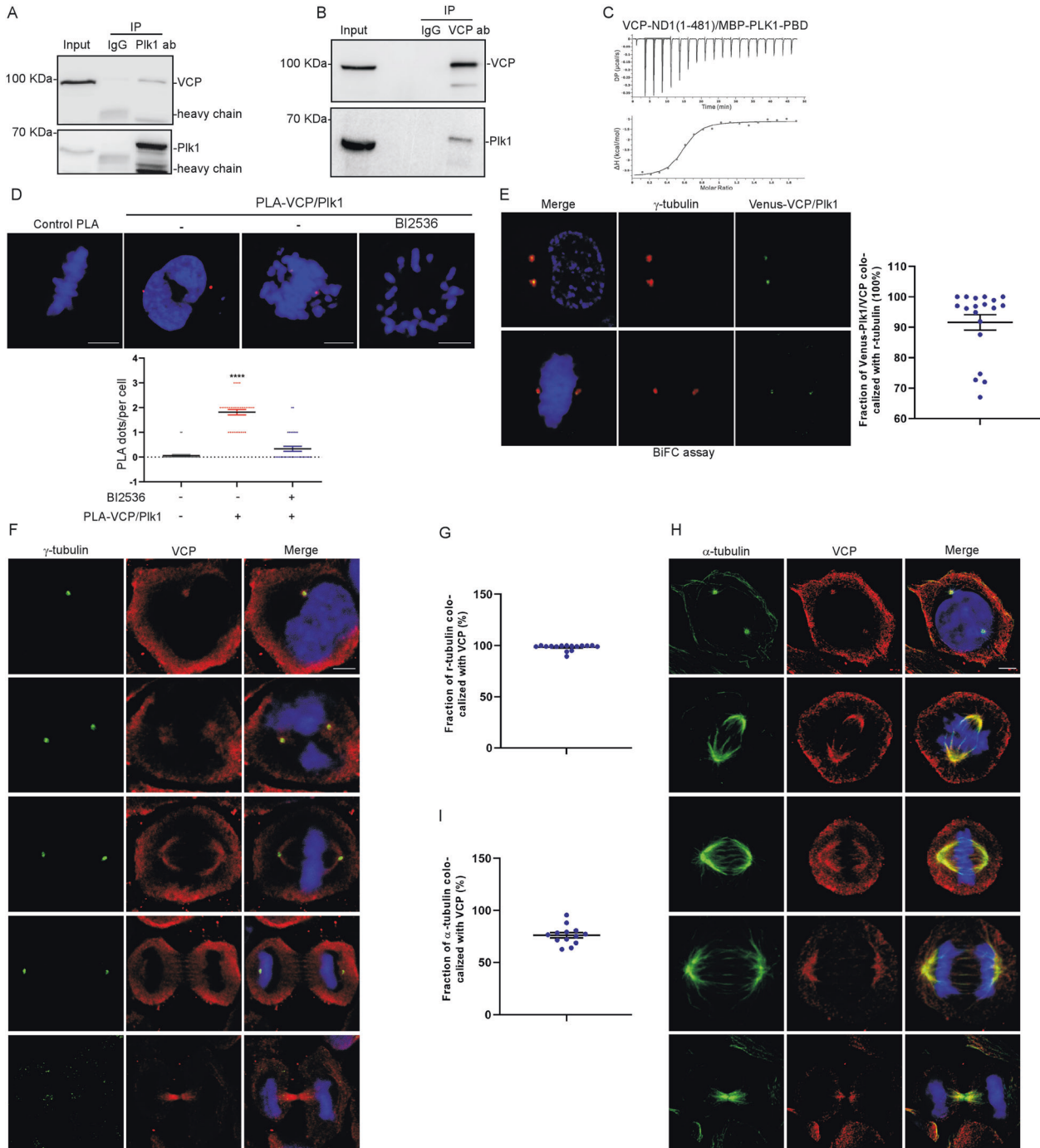


**Fig. 1** Plk1 interacts with VCP at centrosome during M phase. **A**, **B** HeLa cells were synchronized to M phase with nocodazole (Noc) treatment. The cell lysates were incubated with IgG, anti-Plk1 antibody (**A**), or anti-VCP antibody (**B**), and Protein A/G beads. The pull-downs were then subjected to immunoblot analysis against VCP or Plk1. **C** The interaction between VCP-ND1(1-481) and MBP-PLK1-PBD was assessed by isothermal titration calorimetry (ITC). **D** 7 h after released from double thymidine block (DTB), HeLa cells were treated with or without Plk1 inhibitor BI2536 (50 nM) for 2 h. The cells were collected for PLA assay against VCP/Plk1. Quantifications for the positive PLA dots/per cells were performed. Scale bar 5  $\mu$ m. **E** Interaction of Plk1 and VCP was assessed by VN-VCP/VC-Plk1 BiFC (green) with  $\gamma$ -tubulin (red) immunofluorescence staining in HeLa cells. Scale bar 5  $\mu$ m. The percentage of Venus-Plk1/VCP puncta that are  $\gamma$ -tubulin positive against total Venus-Plk1/VCP puncta (MCC) in mitotic HeLa cells was quantified. **F–H** HeLa cells were synchronized with DTB and released to M phase. Cells were collected and stained with anti-VCP (red), anti- $\gamma$ -tubulin (green) (**F**) or anti- $\alpha$ -tubulin (green) (**H**) antibodies, and DAPI (blue). Scale bar 5  $\mu$ m. The colocalization coefficients (MCC) between VCP and  $\gamma$ -tubulin (**G**), as well as VCP and  $\alpha$ -tubulin (**I**) in mitotic HeLa cells were quantified. The blots, images, and graphs are representative data from at least three independent experiments. The difference between two groups was analyzed using two-tailed Student's *t* test,  $p < 0.05$  was considered statistically significant. \* $p < 0.05$ , \*\* $p < 0.01$ , \*\*\* $p < 0.001$ , \*\*\*\* $p < 0.0001$ . MCC Manders colocalization coefficient.

lysine 146, and in this way, its motor activity is fine-tuned [17]. However, the detailed mechanisms regarding the regulation of Eg5 on centrosome and spindle remain elusive.

VCP/p97 (also known as Cdc48) contains a globular N-terminal domain, followed by two AAA ATPase domains (called D1 and D2), with a short linker between them, and a short C-terminal tail. VCP mainly functions as a segregase in the form of hexamer, and it is able to associate with various cofactors to participate in a wide variety of cellular processes, ranging from ER-associated degradation, ribosome-associated degradation, endosomal tracking, autophagy, mitochondria-associated degradation, to chromatin-associated degradation [18–20]. The role of VCP or its cofactors in G1 to S phase transition and DNA replication has been documented [21–23], but investigations on the role of VCP in M phase are limited mainly focusing on events, such as spindle alignment, nucleus reformation, Golgi reassembly, spindle disassembly, and cytokinesis [18, 19, 24–30]. Here, we demonstrated that during the M phase, VCP is enriched at both the centrosome and the spindle from prophase to anaphase. In addition, we identified a dynamic phosphorylation and dephosphorylation switch of the Thr76 residue in VCP during M phase, which is mediated by Plk1 and PTEN, respectively. We further showed that this switch participates in the orientation of the centrosome and spindle for faithful chromosome segregation by regulating the spindle localization of Eg5.

## RESULTS

### Plk1 interacts with VCP in centrosome during M phase

To identify the binding proteins of Plk1 in M phase progression, we added the GST-Flag-Plk1 protein (Fig. S1A) into cycloheximide-treated interphase egg extracts and treated the extracts with non-degradable sea urchin cyclin B ( $\Delta 90$ -cyclinB). The addition of  $\Delta 90$ -cyclinB induced the activation of p42MAPK, the phosphorylation of Thr210 in Plk1, and the mobility shift of Plk1 (Fig. S1B). One hour after  $\Delta 90$ -cyclinB addition, we purified the Plk1 complexes by sequential GST and Flag affinity purification, and the final Flag elution was subjected to mass spectrometry analysis (Fig. S1C). A total 87 proteins were identified in the Plk1 complex, including many that were validated as being Plk1 interacting proteins. Interestingly, VCP/p97 was found in the Plk1 complex (Fig. S1D), and we performed co-immunoprecipitation (co-IP) experiments to assess if there might be an interaction between the two. In nocodazole (Noc)-arrested mitotic HeLa cell lysates, an anti-Plk1 antibody pulled down both Plk1 and VCP (Fig. 1A), and an anti-VCP antibody also brought down both VCP and Plk1 (Fig. 1B). Similarly, in mitotic Twin-Strep-Plk1- and Flag-VCP-expressing HEK293T cells, Strep-Tactin beads pulled down both Plk1 and VCP (Fig. S1E), and Plk1 was found in the Flag-VCP immunocomplex (Fig. S1F). In asynchronous Twin-Strep-Plk1- and Flag-VCP-expressing HEK293T cells, Strep-Tactin beads also pulled down both Plk1 and VCP (Fig. S1G). BI2536 (a Plk1 inhibitor) treatment markedly decreased the interaction between Plk1 and VCP (Fig. S1H). Isothermal titration calorimetry (ITC) also confirmed the interaction between VCP-ND1(1–481) and the MBP-PLK1-PBD domain (367–603) and the dissociation constant (KD) between them was  $\sim 0.915 \pm 0.234 \mu\text{M}$  (Fig. 1C). VCP-ND1 showed very weak binding to MBP protein alone (Fig. S1I). Of note, Plk1 was previously found to be one of 288 putative interacting proteins in VCP immunocomplex [31].

Proteomic screen and structural studies indicate that the core consensus motif recognized by Plk1's PBD is S-pT/pS-P/X by [32, 33]. VCP contains two such motifs in T14 and T613, and interestingly, VCP<sup>T14A</sup> or VCP<sup>T613A</sup> mutant was still found in the Plk1 complex (Fig. S1J). We, thus, verified the interaction between endogenous Plk1 and VCP by performing proximity ligation assays (PLA) in HeLa cells [34]. Two distinct dots, resembling centrosomes, appeared in both late G2 and mitotic HeLa cells, but not in

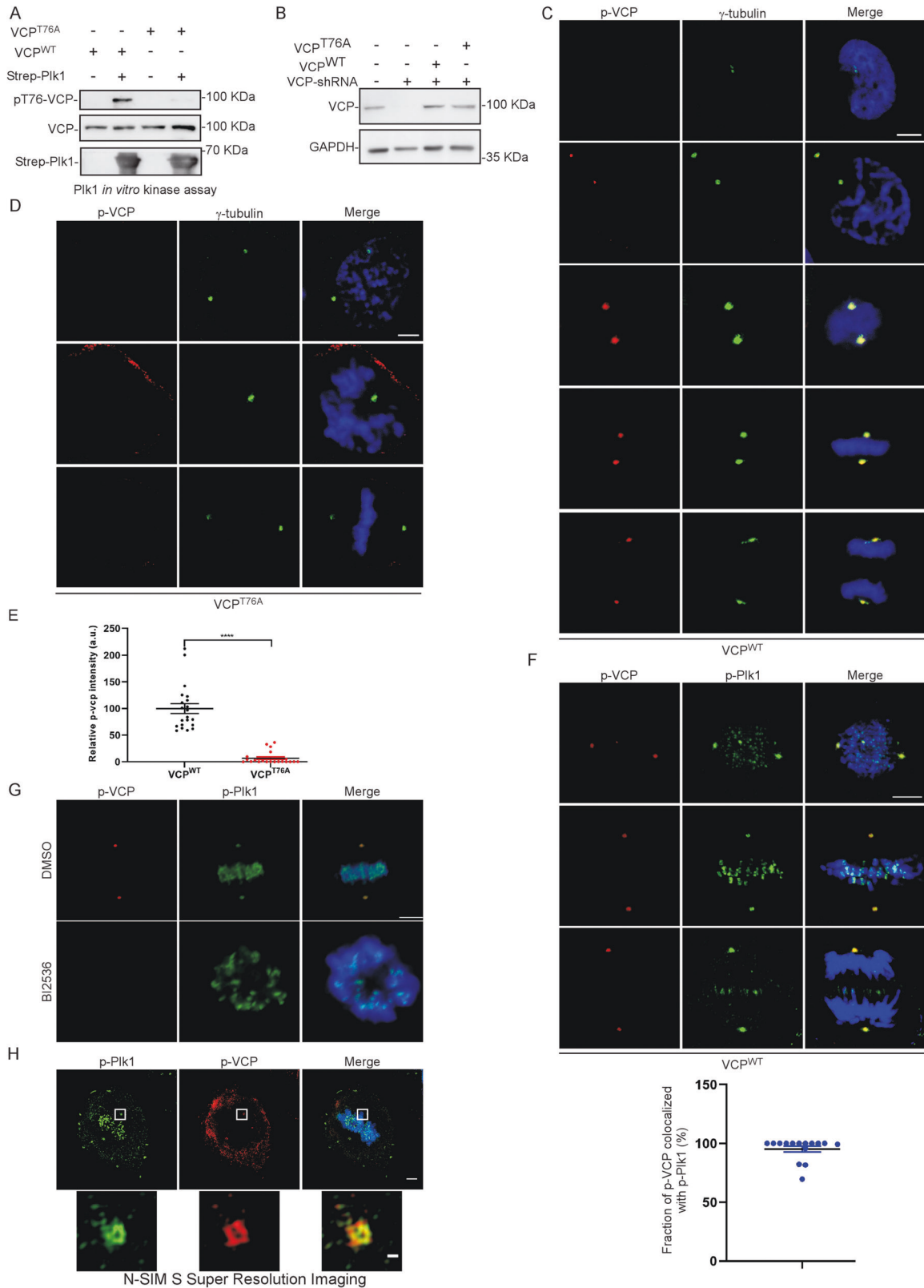
the secondary antibody control cells, which had been treated with all the reagents except the primary antibodies. Also, BI2536 significantly decreased positive PLA signals in mitotic HeLa cells (Fig. 1D). We then assessed whether Plk1 might interact with VCP at the centrosomes in HeLa cells with the bimolecular fluorescence complementation (BiFC) assay [35]. Indeed, specific VN-VCP/VC-Plk1 BiFC signals were detected in both late G2 and mitotic HeLa cells, which co-localized well with  $\gamma$ -tubulin, a centrosomal marker protein (Fig. 1E). Therefore, these data indicate that Plk1 interacts with VCP at the centrosomes during M phase.

We subsequently assessed whether VCP is indeed localized at centrosome during M phase by double immunofluorescence staining of VCP and either  $\gamma$ -tubulin or  $\alpha$ -tubulin. Unexpectedly, VCP was found to be enriched not only at the centrosome, but also at the spindle from prophase to cytokinesis in HeLa cells (Figs. 1F–I and S1K, L). In summary, these data indicate that VCP is associated with both centrosome and spindle during M phase.

### Plk1 phosphorylates the Thr76 residue in VCP at the centrosome during M phase

D/E-X-S/T- $\Phi$ -X-D/E (such that X is any amino acid and  $\Phi$  is a hydrophobic amino acid) has previously been identified as an optimal Plk1 phosphorylation motif [32, 36]. As VCP contains such a potential Plk1 phosphorylation site, (i.e., Thr76) (Fig. S2A), it is possible that Plk1 phosphorylates VCP during M phase. We showed that in the lysate of HeLa cells, VCP exhibited a mobility shift within 9–10 h after being released from double thymidine block (DTB), and this mobility shift was abolished by  $\lambda$ -PPase treatment (Fig. S2B), suggesting that VCP might be phosphorylated during M phase. To test this, we generated an antibody that specifically recognizes VCP phosphorylated at Thr 76 (pT76-VCP). The level of pT76-VCP was increased in Noc-arrested mitotic HeLa cells when compared with that in asynchronous cells or in mitotic cells treated with the Plk1 inhibitor, BI2536. Treatment of Noc-arrested HeLa cell extract with  $\lambda$ -PPase also diminished the level of pT76-VCP (Fig. S2C). We then performed an in vitro Plk1 kinase assay by incubating Twin-Strep-Plk1, which was purified from Noc-arrested HEK293T cells, with recombinant VCP<sup>WT</sup> or VCP<sup>T76A</sup> proteins purified from *E. coli* in kinase reaction buffer, followed by phospho-VCP (T76) immunoblotting. We showed that in vitro, mitotic Plk1 indeed phosphorylated VCP<sup>WT</sup>, but not the VCP<sup>T76A</sup> mutant (Fig. 2A). Likewise, pretreatment of the mitotic Strep-Plk1 with BI2536 markedly inhibited the level of pT76-VCP (Fig. S2D).

Since Plk1 was found to be co-localized with VCP at the centrosomes (Fig. 1D, E), we investigated if Plk1 phosphorylates the Thr76 residue of VCP at the centrosome by performing dual-immunofluorescence staining with the anti-phospho-VCP (T76) and anti- $\gamma$ -tubulin antibodies in HeLa cells. We found that the pT76-VCP signal was specifically detected at the centrosome from prophase to anaphase in HeLa cells (Fig. S2E). To validate the specificity of anti-phospho-VCP (T76) staining at centrosome, we first knocked down the endogenous VCP in HeLa cells with a VCP-specific shRNA and reconstituted the expression of VCP by infecting these cells with a lentivirus encoding shRNA-resistant Flag-VCP<sup>WT</sup> or Flag-VCP<sup>T76A</sup> (Figs. 2B and S2F). Since VCP, one of the most abundant proteins in eukaryotic cells which accounts for close to 1% of total cytoplasmic proteins, is essential for cell viability [37], VCP-knockdown cells almost completely died 72 h after VCP-shRNA lentivirus infection, and only the reconstitution of shRNA-resistant VCP back to the knockdown cells rescued the defects in cell viability (Fig. S2F). As expected, the pT76-VCP signal was consistently detected at the centrosome in VCP<sup>WT</sup>-reconstituted HeLa cells (Fig. 2C, E), similar to that in control HeLa cells (Fig. S2E). In contrast, no pT76-VCP signal was detected at the centrosome in VCP<sup>T76A</sup>-reconstituted cells (Fig. 2D, E). We also transiently transfected HeLa cells with VCP siRNAs to knock down the expression of VCP, and showed that no positive pT76-VCP



signals were detected at centrosomes in mitotic VCP-knockdown cells (Fig. S2G). Likewise, we performed the same dual-immunofluorescence staining experiments in a variety of human and mouse cancer cell lines, and found that the pT76-VCP signal was specifically localized at the centrosome during M phase in all

these cells (Fig. S2H–K). In addition, we performed dual-immunofluorescence staining with anti-phospho-VCP (T76) and anti-phospho-Plk1 (T210) antibodies, and found that although active Plk1 was enriched at both centrosome, kinetochore, and midbody in M phase cells, there was only strong co-localization

**Fig. 2 Plk1 phosphorylates the Thr76 residue in VCP during M phase.** **A** Twin-Strep-Plk1, purified from Noc-arrested Twin-Strep-Plk1-overexpressing HEK293T cell lysates, the Strep beads were washed three times with 1 M NaCl + 0.5% CA630 and once with the in vitro kinase buffer, then incubated with recombinant VCP<sup>WT</sup> or VCP<sup>T76A</sup> protein in the kinase reaction buffer for 1 h followed by phospho-VCP (T76) immunoblotting. **B** The knockdown of VCP with shRNA and the reconstitution of shRNA-resistant VCP<sup>WT</sup> or VCP<sup>T76A</sup> in HeLa cells were assessed by VCP immunoblotting. **C–E** VCP<sup>WT</sup>- (C) or VCP<sup>T76A</sup>-reconstituted (D) HeLa cells were synchronized to M phase with DTB release and stained with anti-phospho-VCP (T76) (red), anti- $\gamma$ -tubulin (green) antibodies, and DAPI (blue). The relative intensity of p-VCP at the centrosome in VCP<sup>WT</sup> and VCP<sup>T76A</sup> cells was quantified (E). Scale bar 5  $\mu$ m. After 7 or 9 h release from DTB, HeLa cells were treated without (F) or with BI2536 (50 nM), a Plk1 inhibitor (G), and stained with anti-phospho-VCP (T76) (red), anti-phospho-Plk1 (T210) (green) antibodies, and DAPI (blue). The colocalization coefficients (MCC) between p-VCP and p-Plk1 in HeLa (F) were quantified. Scale bar 5  $\mu$ m. **H** The N-SIM S Super-resolution imaging of phospho-VCP (T76) and phospho-Plk1 (T210) staining of mitotic HeLa cells. Scale bar for upper panels, 0.5  $\mu$ m for lower panels. The blots, images, and graphs are representative data from at least three independent experiments. MCC Manders colocalization coefficient.

between active Plk1 and pT76-VCP at the centrosome and only from prophase to anaphase (Fig. 2F). Treatment of mitotic HeLa cells with BI2536 abolished the centrosomal pT76-VCP signal (Figs. 2G and S2L). Likewise, knocking down Plk1 via two distinct siRNAs abolished p-T76-VCP signals in mitotic cells (Fig. S2M, N). Of note, Plk1 knockdown also resulted in the asymmetric spindle, such that the spindle poles were in different z planes in Plk1-knockdown cells (Fig. S2M). We further performed N-SIM S super-resolution imaging of the HeLa cells co-immunostained with the anti-phospho-VCP (T76) and anti-phospho-Plk1 (T210) antibodies, and confirmed the co-localization of pT76-VCP with active Plk1 at the centrosome (Fig. 2G). We also assessed whether other mitotic kinases are involved in the phosphorylation of Thr76-VCP. Interestingly, although Barasertib (an Aurora B inhibitor) or CFI-400945 (a Plk4 inhibitor) had no effects on pT76-VCP, Alisertib (an Aurora A inhibitor) treatment of mitotic cells decreased pT76-VCP signals at the centrosome (Fig. S2O, P). Of note, Aurora A has been shown to participate in the activation of Plk1 during mitosis [38, 39]. Indeed, treatment of mitotic cells with Alisertib markedly decreased mitotic phospho-Plk1 levels (Fig. S2Q). Interestingly, in VCP<sup>T76A</sup>-reconstituted HeLa cells, the localization of Plk1 in mitotic cells was not affected (Fig. S2R). Taken together, these data demonstrate that Plk1 phosphorylates the Thr76 residue in VCP at the centrosome during the M phase.

### VCP-Thr76 phosphorylation is important for chromosome segregation and the orientation of the centrosome and spindle

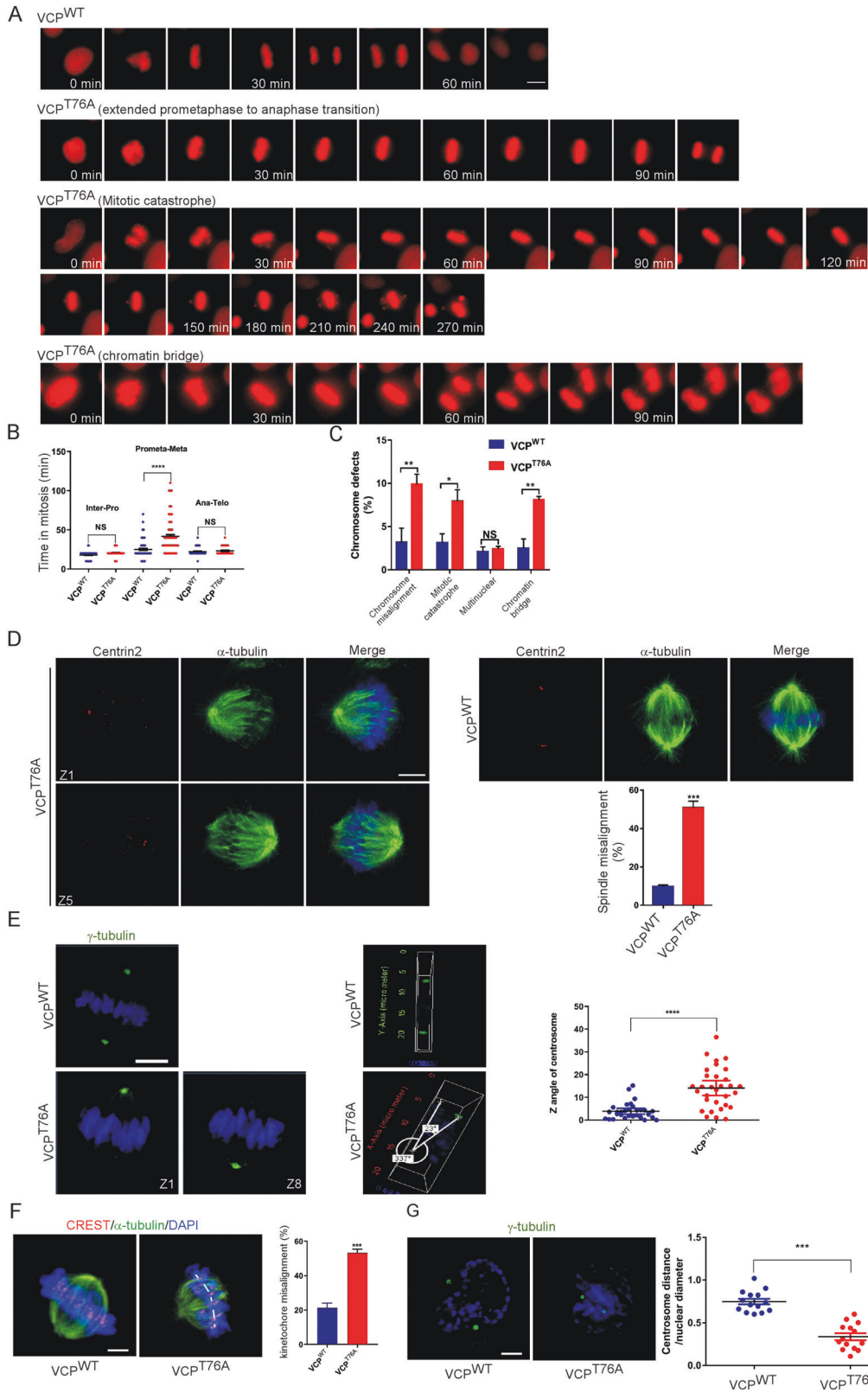
Since Plk1 phosphorylates Thr76 residue in VCP in mitotic cells (Figs. 2 and S2), we investigated the role of this phosphorylation in M phase progression. The Flag-VCP<sup>WT</sup>- or Flag-VCP<sup>T76A</sup>-reconstituted HeLa cells (Fig. 2B) were synchronized by DTB at the G1/S boundary, released into the normal medium, collected at different time points, and stained with propidium iodide (PI), followed by flow cytometric analysis. The levels of the Flag-VCP<sup>WT</sup> or Flag-VCP<sup>T76A</sup> in these reconstituted cells were similar to the endogenous VCP in control cells (Fig. 2B). The Flag-VCP<sup>WT</sup>-reconstituted cells exhibited a similar cell cycle progression pattern as control HeLa cells (Fig. S3A). Although no defects in M phase entry were identified in the Flag-VCP<sup>T76A</sup>-reconstituted cells, they appeared to stay at the M phase longer than the control cells (Fig. S3A, B). To more accurately measure the mitotic index, we infected the Flag-VCP<sup>WT</sup>- or Flag-VCP<sup>T76A</sup>-reconstituted HeLa cells with a lentivirus encoding H2B-RFP, and performed live-cell fluorescence imaging to monitor their M phase progression (Supplementary Videos 1 and 2). Consistently, the Flag-VCP<sup>T76A</sup>-reconstituted cells spent significantly longer completing chromosome segregation (from prophase to the onset of anaphase) than the Flag-VCP<sup>WT</sup>-reconstituted cells (Fig. 3A, B). A significant number of Flag-VCP<sup>T76A</sup>-reconstituted cells also exhibited multiple chromosome defects (e.g., mitotic catastrophe, chromatin bridge, and chromosome misalignment), than the Flag-VCP<sup>WT</sup>-reconstituted cells (Fig. 3A, C). These data suggest that the phosphorylation of VCP Thr76 is involved in chromosome segregation.

Since the mitotic spindle is responsible for chromosome alignment and segregation during M phase, we next characterized the morphology and orientation of the spindle in Flag-VCP<sup>T76A</sup>-reconstituted HeLa cells by immunofluorescence staining of centrin-2 (a structural protein of the centrosome) and  $\alpha$ -tubulin, followed by confocal planar z section analysis. In most of the Flag-VCP<sup>WT</sup>-reconstituted cells, the mitotic spindle was symmetric. The two spindle poles (located at opposite sides of the cell) were in similar z planes at 9 h after DTB release. In contrast, in a significant number of Flag-VCP<sup>T76A</sup>-reconstituted cells, the mitotic spindle was asymmetric, such that the spindle poles were in different z planes at 9 h after DTB release (Figs. 3D and S3C, D). The spindle angle, obtained by measuring the z angles of the centrosomes in the  $\gamma$ -tubulin staining cells, was also significantly larger in the Flag-VCP<sup>T76A</sup>-reconstituted cells than in the control cells (Fig. 3E), again confirming the misaligned spindle in VCP<sup>T76A</sup>-reconstituted cells. Likewise, analysis of CREST (anti-kinetochore antibody) and anti- $\alpha$ -tubulin dual-immunolabeled cells, indicated that a significant portion of the Flag-VCP<sup>T76A</sup>-reconstituted cells (~55%) exhibited kinetochore misalignment defects when compared with the Flag-VCP<sup>WT</sup>-reconstituted cells (Figs. 3F and S3E). In addition, in the late G2 phase and after nuclear envelope breakdown, the centrosome ( $\gamma$ -tubulin) distance was significantly shorter in the Flag-VCP<sup>T76A</sup>-reconstituted cells than in the Flag-VCP<sup>WT</sup>-reconstituted cells (Figs. 3G and S3F). Notably, similar defects have been reported in Plk1 knockdown cells [40–42]. Taken together, these data indicate that the phosphorylation of Thr76 in VCP, mediated by Plk1, is required for proper orientation of centrosome and spindle, and chromosome segregation.

We speculated that the observed asymmetric spindle and/or misaligned kinetochore in VCP<sup>T76A</sup>-reconstituted cells (Figs. 3D–F and S3D–F) might activate SAC to delay chromosome segregation and prolong the M phase (Figs. 3A–C and S3A, B) until cells correct these defects. Therefore, VCP<sup>WT</sup>- or VCP<sup>T76A</sup>-reconstituted HeLa cells were arrested in metaphase after being released from DTB in the presence of MG132 (a proteasome inhibitor). These cells were then stained with anti-Mad2 antibody and DAPI. MAD2 was used as a marker for unattached kinetochores [43]. We showed that the percentage of Mad2-positive VCP<sup>T76A</sup>-reconstituted cells is significantly higher when compared to that in VCP<sup>WT</sup>-reconstituted cells (left panel in Fig. S3G). As a positive control, treatment of VCP<sup>WT</sup>- or VCP<sup>T76A</sup>-reconstituted cells with Eg5 inhibitor fully activated SAC in both cells (right panel in Fig. S3G). Collectively, these results suggest that SAC is activated in most VCP<sup>T76A</sup>-reconstituted cells.

### The phosphorylation of VCP Thr76 is required for the recruitment of VCP and Eg5 to the centrosome

To further understand the role of VCP in spindle orientation, we generated a BioID-VCP-expressing HeLa cell line (Fig. S4A). BioID2 is a promiscuous biotin ligase, which biotinylates proteins that are the near-neighbors of the fusion protein under investigation in a proximity-dependent manner in living cells [44]. We enriched the number of mitotic BioID-VCP-expressing cells with the



Noc-treatment in the presence of biotin, and identified the biotinylated proteins in these cells via affinity purification and mass spectrometry analysis. A total of 150 potential VCP binding proteins were identified, including many VCP cofactors and known substrates (Fig. S4B). Interestingly, Kinesin 5 (Eg5; also known as

KIF11) was found in the VCP complex. Here we verified the interaction between VCP and Eg5 with co-IP experiments (Fig. 4A, B). We then conducted dual-immunofluorescence staining experiments with the anti-Eg5 and anti- $\alpha$ -tubulin antibodies to assess if the expression of Eg5 in the centrosome or spindle might be

**Fig. 3 VCP-Thr76 phosphorylation is required for chromosome segregation, M phase progression, and centrosome and spindle orientation.** **A–C** The mitotic progression in RFP-H2B-expressing VCP<sup>WT</sup> or VCP<sup>T76A</sup>-HeLa cells was monitored by time-lapse microscopy. The representative frames showing cells with normal or extended M phase, or cells with chromosome defects were shown for comparison (**A**). The time of the cells spent at different phases in mitosis (**B**) and the various chromosome defects of the cells in the M phase (**C**) were quantified. **D** VCP<sup>WT</sup>- or VCP<sup>T76A</sup>-reconstituted HeLa cells were stained with anti-Centrin2 (red) and anti- $\alpha$ -tubulin (green) antibodies, and DAPI (blue) followed by confocal planar z section analysis. Representative images of z sections were shown, and the percentage of spindle misalignment cells was quantified. **E** VCP<sup>WT</sup>- or VCP<sup>T76A</sup>-reconstituted HeLa cells were stained with anti- $\gamma$ -tubulin (green) antibody and DAPI (blue) followed by confocal planar z section analysis. Representative images of z sections were shown, and the average z angle of centrosomes was quantified. **F** VCP<sup>WT</sup>- or VCP<sup>T76A</sup>-reconstituted HeLa cells were stained with CREST (red) and anti- $\alpha$ -tubulin (green) antibodies, and DAPI (blue). The percentage of cells with misaligned chromosomes was quantified. **G** VCP<sup>WT</sup>- or VCP<sup>T76A</sup>-reconstituted HeLa cells were stained with anti- $\gamma$ -tubulin (green) antibody and DAPI (blue). The centrosomes distance was quantified over nuclear diameter. Scale bar 5  $\mu$ m. The images and graphs are representative data from at least three independent experiments. The difference between two groups was analyzed using two-tailed Student's *t* test, *p* < 0.05 was considered statistically significant. \**p* < 0.05, \*\**p* < 0.01, \*\*\**p* < 0.001, \*\*\*\**p* < 0.0001.

affected in VCP<sup>T76A</sup>-reconstituted cells. Indeed, the mean intensity of Eg5 at centrosome and spindle in the Flag-VCP<sup>T76A</sup>-reconstituted cells was significantly decreased when compared with that in Flag-VCP<sup>WT</sup>-reconstituted cells (Figs. 4C–E and S4C). Likewise, the anti-Flag antibody pulled down Eg5 only from the mitotic Flag-VCP<sup>WT</sup>-reconstituted cells, but not from the Flag-VCP<sup>T76A</sup>-reconstituted cells (Fig. 4B).

Since Plk1 was shown to be responsible for the phosphorylation of Thr76 in VCP (Fig. 2), we treated mitotic cells with BI2536, and then dual-immunostained them with the anti-Eg5 and anti-VCP antibodies. As expected, the accumulation of Eg5 at the centrosome and spindle was diminished by BI2536 treatment. Unexpectedly, BI2536 abolished the localization of VCP at the spindle as well as at the centrosome (Fig. 4F–H). Since Plk1 is not associated with the spindle, this suggests that centrosomal p76-VCP and spindle-unphosphorylated VCP might be interconnected. To investigate if this might be the case, we stained the Flag-VCP<sup>WT</sup>- or Flag-VCP<sup>T76A</sup>-reconstituted HeLa cells with anti-VCP antibody. We found that VCP only exhibited strong co-localization with  $\alpha$ -tubulin in Flag-VCP<sup>WT</sup>-reconstituted cells, and the spindle-associated VCP staining was significantly decreased in Flag-VCP<sup>T76A</sup>-reconstituted cells (Figs. 4I and S5A). The localization of Eg5 at spindle, and the orientation of centrosome and spindle were also compromised by DBeQ or CB5083 (VCP inhibitors) (Fig. S5B–D). In summary, these results suggest that the recruitment of VCP to the spindle relies on the phosphorylation of Thr76 by Plk1, and that centrosomal VCP promotes the localization of Eg5 at the spindle to ensure faithful centrosome orientation.

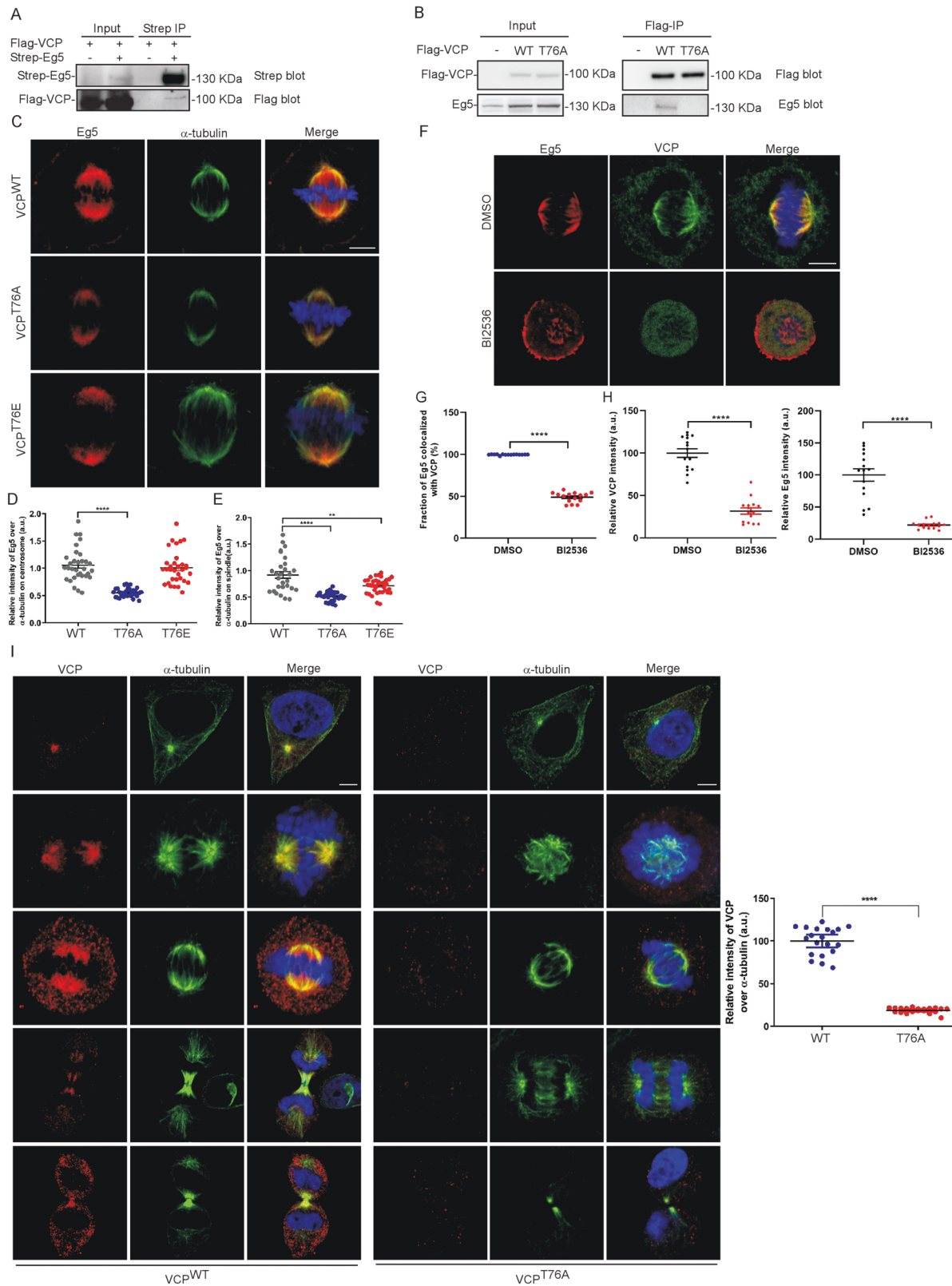
Of note, the total cellular ubiquitination levels in the Flag-VCP<sup>T76A</sup>-reconstituted cells were similar to those in the Flag-VCP<sup>WT</sup>-reconstituted cells; however, the treatment of cells with CB5083 markedly induced the accumulation of either ubiquitinated proteins or NRF1 (a VCP-mediated degradation substrate), in cells (Fig. S5E). Similarly, CCAAT/enhancer-binding protein homologous protein (CHOP), whose expression is markedly induced by ER stress [45], was undetectable in the VCP<sup>WT</sup>- or VCP<sup>T76A</sup>-reconstituted cells, and CB5083 treatment significantly induced CHOP expression in these cells (Fig. S5F, G). Therefore, these results suggest that the T76 mutations do not change the well-established VCP function related to its ATPase activity.

#### PTEN is required for VCP Thr76 dephosphorylation during M phase

VCP was not enriched at spindle in VCP<sup>T76A</sup>-reconstituted HeLa cells (Figs. 4I and S5A), and the Thr76 in spindle-associated VCP in control or VCP<sup>WT</sup>-reconstituted HeLa cells is not phosphorylated (Figs. 2C and S2E). This suggests that Thr76 is dephosphorylated when VCP is moved to the spindle. We, therefore, investigated whether dephosphorylation of pT76-VCP is required for the spindle accumulation of VCP. We mutated the Thr76 in VCP to glutamic acid to mimic phosphorylation, and then reconstituted the expression of VCP by infecting the VCP-knockdown HeLa cells with a lentivirus encoding shRNA-resistant Flag-VCP<sup>T76E</sup> (Fig. S6A).

As expected, in these Flag-VCP<sup>T76E</sup>-reconstituted cells, VCP lost its spindle localization, but it was enriched at the spindle pole during M phase (Fig. S6B). Eg5 levels at the spindle, not the centrosome, in VCP<sup>T76E</sup>-reconstituted cells were also significantly lower when compared to VCP<sup>WT</sup>-reconstituted cells (Fig. 4C–E). Likewise, the spindle pole was fragmented in a significant proportion (~40%) of the Flag-VCP<sup>T76E</sup>-reconstituted cells when compared with the control cells (Fig. S6C, D). The z angles of the centrosomes in the  $\gamma$ -tubulin staining cells were also significantly larger in the VCP<sup>T76E</sup>-reconstituted cells than in the control cells (Fig. S6E, F). We infected the Flag-VCP<sup>T76E</sup>-reconstituted HeLa cells with a lentivirus encoding H2B-RFP, and performed live-cell fluorescence imaging to monitor M phase progression (Supplementary Video 3). The Flag-VCP<sup>T76E</sup>-reconstituted cells spent significantly longer to complete chromosome segregation than the control cells (Fig. S6G). A significant number of Flag-VCP<sup>T76E</sup>-reconstituted cells exhibited chromatin bridge and chromosome misalignment, when compared to the control cells (Fig. S6H, I). Again, these data indicate that the dephosphorylation of Thr76 in VCP (like its phosphorylation at the centrosome by Plk1), is required for the recruitment of VCP to the spindle in M phase, and participates in M phase progression. Of note, the defects caused by T76A are more severe than T76E (comparing Fig. 3 to Fig. S6). We speculate that this is because T76A mutation completely abolished VCP localization to both centrosome and spindle, whereas T76E mutation only affected VCP enrichment at the spindle.

We then investigated which specific phosphatase is responsible for the dephosphorylation of Thr76 in VCP at the spindle. We generated siRNA pools to individually knock down seven of the mitotic phosphatases reported in the literature. These were six protein serine/threonine phosphatases (PP1 $\alpha$ , PP1 $\beta$ , PP1 $\gamma$ , PP2A, PP4, and PP6), and PTEN. The knockdown efficiency was then verified by RT-qPCR (Fig. S7A). Interestingly, only PTEN knockdown blocked the enrichment of VCP to the spindle (Fig. S7B). To validate these siRNA knockdown data, we treated DTB-released HeLa cells (i.e., ~7 to 9 h after release) with okadaic acid, a potent PP1 and PP2A inhibitor [46], and found that it had little effect on the recruitment of VCP or Eg5 to the spindle in M phase (Fig. S7C). We also designed two PTEN specific sgRNAs and knocked down the expression of PTEN in HeLa cells by CRISPR/Cas9 (Fig. 5A). Although the knockdown of PTEN with these various sgRNAs abolished the recruitment of VCP to the spindle in M phase cells (Fig. 5B), it also enhanced the pT76-VCP signals at the centrosome (Fig. 5C). Similarly, VCP was not found in the spindle in mitotic PTEN-deficient PC3 cells (Fig. S7D). We then performed the aforementioned *in vitro* Plk1 kinase assay using VCP as the substrate, and the phosphorylated VCP was subsequently incubated with HA-PTEN, which was immuno-purified from HA-PTEN-overexpressing HEK293T cells treated with Noc, followed by phospho-VCP (T76) immunoblotting. The HA-PTEN indeed abolished the pT76-VCP signal (Fig. 5D). We performed co-IP experiments to assess if PTEN interacts with VCP. When cells were co-transfected with both HA-PTEN<sup>WT</sup> and Twin-Strep-VCP, Strep-



Tactin beads pulled down both Twin-Step-VCP and HA-PTEN<sup>WT</sup>. Interestingly, when cells were co-transfected with both Twin-strep-VCP and HA-PTEN<sup>C124S</sup>, the latter being a phosphatase dead mutant [47], Strep-Tactin beads failed to pull down PTEN<sup>C124S</sup>

(Fig. 5E). Collectively, these data demonstrate that PTEN is required for the dephosphorylation of Thr76 in VCP during M phase progression, and that this dephosphorylation is essential for the recruitment of VCP to the spindle.



**Fig. 4 The phosphorylation of VCP-Thr76 is required for the recruitment of VCP and Eg5 to the centrosome.** **A** HEK293T cells were transiently transfected with Flag-VCP and/or Twin-Strep-Eg5, and were then synchronized to M phase with Noc treatment. The cell lysates were incubated with Strep-Tactin® Sepharose, and the pulldowns were subjected to immunoblot analysis against Flag or Strep. **B** Flag-VCP<sup>WT</sup>- or Flag-VCP<sup>T76A</sup>-reconstituted HeLa cells were synchronized to M phase with Noc treatment and subjected to Flag IP. The cell lysates were incubated with FLAG® M2 Magnetic Beads, and the pulldowns were subjected to immunoblot analysis against Flag or Eg5. **C–E** VCP<sup>WT</sup> or VCP<sup>T76A</sup>-reconstituted HeLa cells were stained with anti-Eg5 (red) and anti- $\alpha$ -tubulin (green) antibodies, and DAPI (blue). Scale bar 5  $\mu$ m. **C** The relative Eg5 intensities at centrosome **(D)** or spindle **(E)** were quantified. **F–H** HeLa cells treated with Plk1 inhibitor BI2536 (50 nM) were stained with anti-Eg5 (red), anti-VCP (green) antibodies, and DAPI (blue) **(F)**. The percentage of Eg5 that are VCP positive against total Eg5 puncta (MCC) in mitotic HeLa cells treated with or without BI2636 was quantified by MCC **(G)**. Also, the relative fluorescence intensities Eg5 or VCP in mitotic HeLa cells treated with or without BI2636 were quantified **(H)**. **I** VCP<sup>WT</sup>- or VCP<sup>T76A</sup>-reconstituted HeLa cells were synchronized with DTB and released to M phase. Cells were collected and stained with anti-VCP (red), anti- $\alpha$ -tubulin (green) antibodies, and DAPI (blue). Scale bar 5  $\mu$ m. The relative VCP fluorescence intensity over  $\alpha$ -tubulin staining was quantified. The blots, images, and graphs are representative data from at least three independent experiments. The difference between two groups was analyzed using two-tailed Student's *t* test, *p* < 0.05 was considered statistically significant. \**p* < 0.05, \*\**p* < 0.01, \*\*\**p* < 0.001, \*\*\*\**p* < 0.0001.

### T76 mutations influence inter-subunit communication of VCP

VCP mainly regulates various cellular events via the ATPase activity of its D1-D2 domains and the cofactor binding activity of its N-terminal domain. However, the ATPase activities of full-length VCP<sup>T76A</sup> and VCP<sup>T76E</sup> proteins, representing the dephosphorylated and phosphorylated states, respectively, were similar to wild-type VCP protein (Fig. S8A). To investigate the effects of T76 phosphorylation on structure change of VCP, we acquired the cryo-EM structures of VCP<sup>T76A</sup> and VCP<sup>T76E</sup> in the presence of ADP and AMP-PNP (an ATP analog), respectively. When compared with previously reported structures of wild-type VCP (PDB code 5ftk and 5ftm) [48], VCP<sup>T76A</sup> and VCP<sup>T76E</sup> did not show any dramatic overall structural changes (Fig. S8B, C). Structural superposition indicated that the monomeric forms of VCP<sup>T76A</sup>, VCP<sup>T76E</sup>, and VCP<sup>WT</sup> are all very similar (Fig. S8D–F). This is comparable to our new findings and a previous report on IBMPFD pathogenic mutations (Fig. S8G, H) [49]. However, we did observe subtle differences in the inter-subunit interactions between the nucleotide-binding pocket of one subunit and the arginine finger of an adjacent subunit, which is essential for both the nucleotide-binding of VCP [49, 50]. This arginine finger motif (called the SRH motif), is a defining feature of the AAA + ATPase family. The SRH motif for the D1 domain of VCP is known as <sup>359</sup>RFGR<sup>362</sup>. In wild-type VCP, both R359 and R362 bind to the  $\beta$ -phosphate of ADP when the ATPase is inactive, and they alter their positions to accommodate the  $\gamma$ -phosphate of ATP when the D1 ATPase exchanges the nucleotide to ATP. We found that in all the VCP<sup>T76A</sup> structures, whether in the ADP- or AMP-PNP-bound form, the whole SRH motif was twisted, which resulted in the dislocation of residue R359 to a direction facing residue N348. The loss of binding with residue R359 in VCP<sup>T76A</sup> caused conformational shifts of ADP or AMP-PNP, and resulted in their terminal phosphate group facing toward residue T252 and binding with T252, R256, and K336 from a neighboring subunit (Fig. 6A–C). In contrast, in the binding pocket of VCP<sup>T76E</sup>, the  $\beta$ -phosphate moiety of the bound nucleotide faces toward residue R359 (Fig. 6D). The conformational variations of the nucleotide-binding pocket provide direct evidence that mutations of T76 affect the nucleotide-binding environment of D1 ATPase by alternating the inter-subunit communication of VCP protein.

To further investigate the mechanism of how the T76 site influences D1 domain, we compared the N-D1 interfaces of VCP<sup>T76A</sup>, VCP<sup>T76E</sup>, and VCP<sup>WT</sup> (PDB: 5ftm) (Fig. 6E). Although the T76 site is located in a flexible loop that hangs below the N-domain and is always exposed to solution, it still manages to influence the N-D1 interface in an indirect way. In both VCP<sup>WT</sup> and VCP<sup>T76E</sup> structures, residues T76 or E76 forms a hydrogen bond with residue R83, but the bond is diminished in VCP<sup>T76A</sup> due to the shift of residue R83 forming a hydrogen bond with residue D29, which results in a slight movement of the helix <sup>86</sup>RVVRAAL<sup>92</sup> and loop <sup>29</sup>DEAINE<sup>34</sup> located at the N-D1 interface. These observations suggest that the T76A mutation eliminates the T76-R83 bond,

which, in turn, influences the inter-domain communication of N-D1 and the inter-subunit communication of the D1 hexamer. In contrast, phosphorylation of residue T76 would strengthen the T76-R83 bond and therefore indirectly promote both inter-domain and inter-subunit communications.

### The VCP T76A mutation suppresses tumor formation in a xenograft mouse model

Since genome instability is the hallmark of cancer and the phosphorylation of Thr76 in VCP is important for proper centrosome movement, spindle orientation, and chromosome segregation (Figs. 3 and S3), we speculate that cancer cells harboring the VCP<sup>T76A</sup> mutation might have a higher tumorigenic ability than VCP<sup>WT</sup>-expressing cells. Thus, we knocked down VCP in MDA-MB-231 cells with its specific shRNA, and reconstituted the expression of VCP by infecting these cells with a lentivirus encoding shRNA-resistant Flag-VCP<sup>WT</sup> or Flag-VCP<sup>T76A</sup> (Fig. 7A). Unexpectedly, the Flag-VCP<sup>T76A</sup>-reconstituted MDA-MB-231 cells grew slower in culture than the Flag-VCP<sup>WT</sup>-reconstituted cells when kept in medium containing 2% FBS, although their growth rates were similar when maintained in complete medium (10% FBS) (Fig. S9A). Likewise, the VCP<sup>T76A</sup>-reconstituted cells were less able to form tumor spheroids when compared with the VCP<sup>WT</sup>-reconstituted cells, which suggests that the VCP<sup>T76A</sup> mutation weakens the tumor-forming ability of cancer cells in vitro (Fig. 7B). We then implanted the VCP<sup>WT</sup>- or VCP<sup>T76A</sup>-reconstituted MDA-MB-231 cells into nude mice, and found that the tumor growth in mice implanted with VCP<sup>T76A</sup>-reconstituted cells was significantly slower when compared with those implanted with VCP<sup>WT</sup>-reconstituted cells (Fig. 7C–E). Of note, p-VCP signals were significantly weaker in VCP<sup>T76A</sup> tumor sections when compared to VCP<sup>WT</sup> tumor sections (Fig. S9B).

To better understand the decreased tumor formation ability of the VCP<sup>T76A</sup>-reconstituted cells, we isolated the primary tumor tissues from the nude mice for RNA-Seq analysis. Of the 57,905 mapped whole-genome genes that were obtained in the isolated tumors, we identified 234 differentially expressed genes (DEGs; false discovery rate (FDR) < 0.1), including 111 downregulated and 123 upregulated genes in the VCP<sup>T76A</sup>-expressing tumors when compared with those in the VCP<sup>WT</sup>-expressing tumors (Fig. S9C, D). Subsequent ingenuity pathway analysis (IPA) of the DEGs revealed that several signaling pathways were significantly affected. These included the TNF, nod-like receptor, IL-17, PI3K-AKT, and MAPK signaling pathways, which are closely related to apoptosis, cell division, and tumor growth (Fig. S9E). Thus, we performed a gene set enrichment analysis using the whole gene list generated from our RNA-seq, and found that the apoptosis pathway was significantly enriched (FDR = 0.05), and the cell cycle pathway and various cancer-related pathways also showed a trend of significance (Figs. 7F and S9F). As expected, many pro-apoptotic genes were upregulated in the VCP<sup>T76A</sup>-expressing tumor tissues when compared with those expressing VCP<sup>WT</sup>

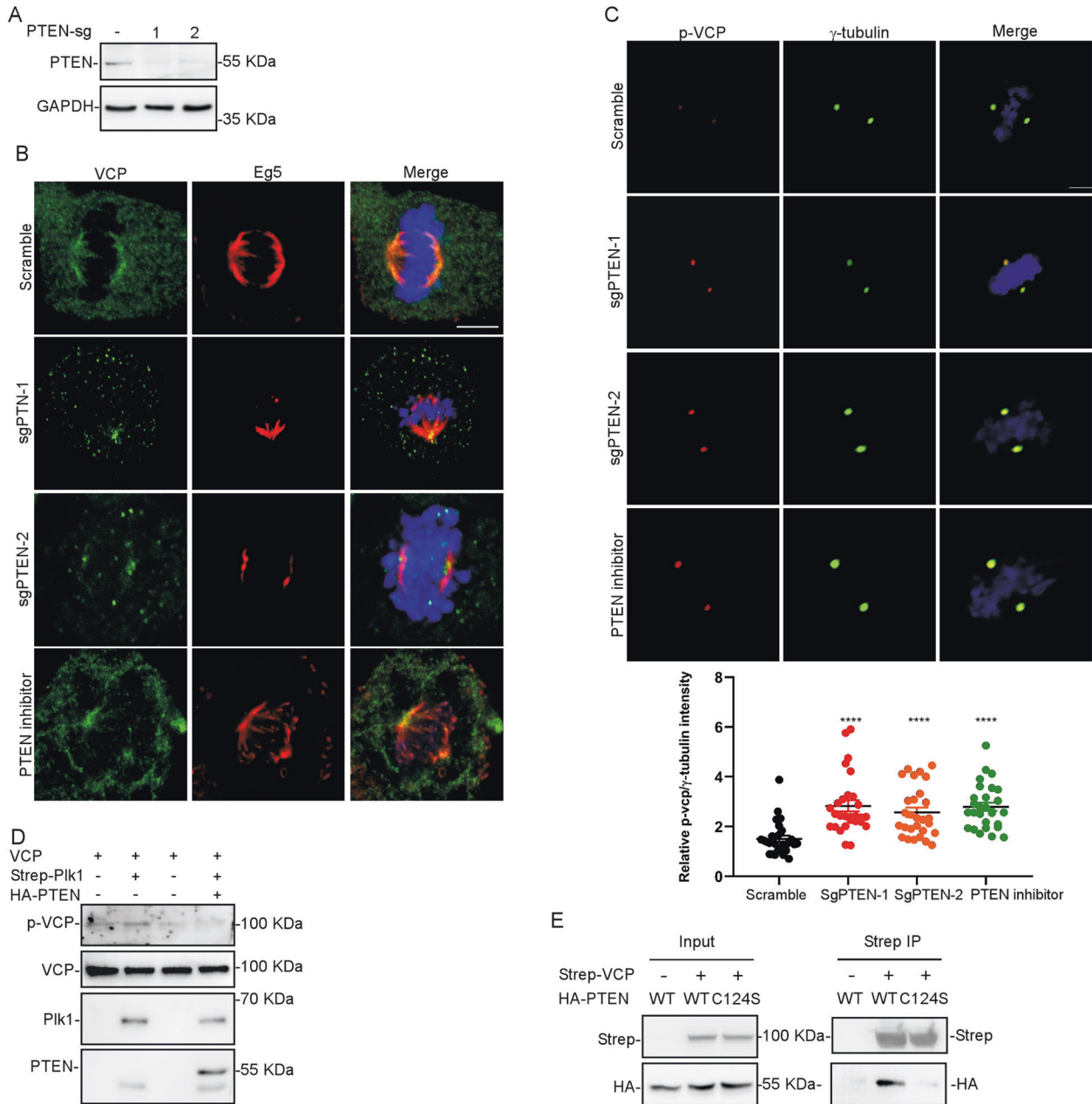


**Fig. 5 PTEN is required for the dephosphorylation of Thr76 in VCP during M phase.** **A** The knockdown of PTEN by two sgRNAs was verified by PTEN immunoblotting. **B, C** Scramble or PTEN knockdown HeLa cells were stained with anti-VCP (green) and anti-Eg5 antibodies (red) (**B**) or with anti-phospho-VCP (T76) (red) and anti- $\gamma$ -tubulin (green) antibodies (**C**). The relative phospho-VCP (T76) fluorescence intensity was qualified over  $\gamma$ -tubulin. Scale bar 5  $\mu$ m. **D** Twin-Strep-Plk1, purified from Noc-treated Twin-Strep-Plk1-overexpressing HEK293T cell lysates, was incubated with recombinant VCP<sup>WT</sup> protein in a kinase reaction buffer for 1 h, and the phosphorylated VCP was subsequently incubated with or without HA-PTEN purified from Noc-treated HA-PTEN-overexpressing HEK293T cells in dephosphorylation buffer and subjected to phospho-VCP (T76) immunoblotting. **E** HEK293T cells were transiently transfected with HA-PTEN<sup>WT</sup> or HA-PTEN<sup>C124S</sup> and/or Twin-Strep-VCP, and were synchronized to M phase with Noc treatment. The cell lysates were incubated with Strep-Tactin® Sepharose, and the pull-downs were subjected to immunoblot analysis against HA or Strep. The blots, images, and graphs are representative data from at least three independent experiments. The difference between two groups was analyzed using two-tailed Student's *t* test,  $p < 0.05$  was considered statistically significant. \* $p < 0.05$ , \*\* $p < 0.01$ , \*\*\* $p < 0.001$ , \*\*\*\* $p < 0.0001$ .

(Figs. 7G and S9F). For example, the tumor suppressor gene, RARRES2, was transcriptionally downregulated in many tumors and was reported to induce cell apoptosis in granulosa cells [51, 52]. Other apoptotic genes, such as LSP1, TGFBI, and HSPB8 [53–55], were also found to be upregulated in the VCP<sup>T76A</sup> tumors (Figs. 7G and S9F). In contrast, several tumor-promoting genes were found to be downregulated in the VCP<sup>T76A</sup>-expressing tumor tissues when compared with the VCP<sup>WT</sup>-expressing tumors

(Fig. 7G). For example, IL1A, IL6, and IL8 were all involved in the tumor microenvironment and could facilitate tumor formation [56–58]. We, therefore, performed the TUNEL assay in primary tumor tissue sections isolated from nude mice, and showed that the proportion of apoptotic cells in the VCP<sup>T76A</sup>-expressing tumor tissues was indeed significantly higher than in the VCP<sup>WT</sup>-expressing tumor tissues (Fig. 7H). In summary, these data indicate that the cells harboring the VCP<sup>T76A</sup> mutation are less

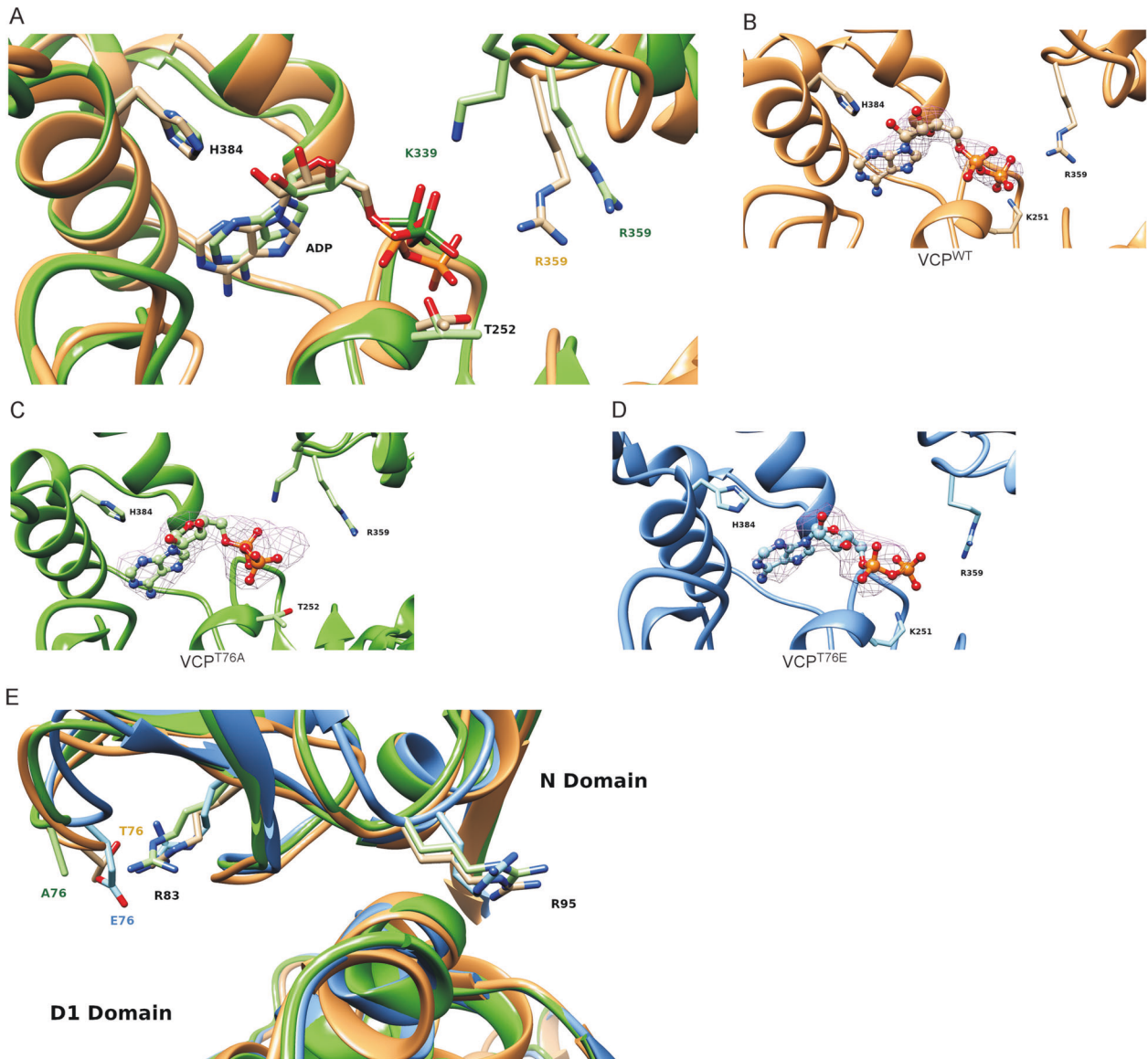


**Fig. 6** T76 mutations influence the ATPase activity and inter-subunit communication of VCP. **A** Detailed comparison between the atomic model of VCP<sup>T76A</sup> AMP-PNP-bound conformation (Green) and VCP<sup>WT</sup> (PDB 5ftm, Orange) around the nucleotide-binding pocket. **B–D** Structures of VCP<sup>WT</sup> (PDB: 5ftm) (**B**), VCP<sup>T76A</sup> (AMP-PNP bound Conformation) (**C**), and VCP<sup>T76E</sup> (AMP-PNP bound Conformation) (**D**) with inactive D1 ATPase, showing the orientation of  $\beta$ -phosphate. **E** Detailed comparison between the atomic models of the N-D1 interface of the AMP-PNP-bound form of VCP<sup>T76A</sup> (Green), VCP<sup>T76E</sup> (Blue) and VCP<sup>WT</sup> (Orange, PDB: 5 ftm).

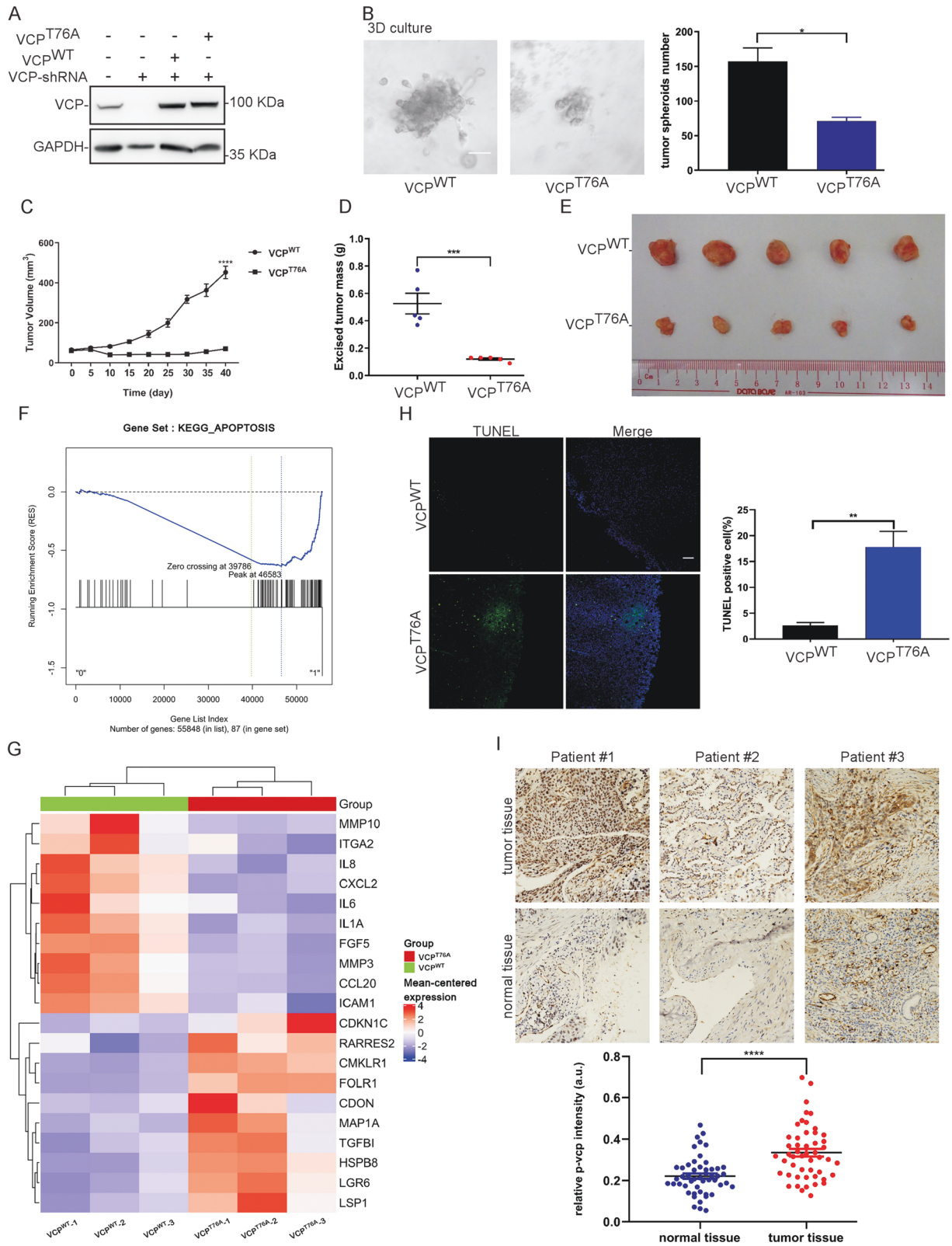
likely to develop into tumors. Along this line, no VCP-T76 mutations were identified in cancer patients (Fig. S9G and Table S1). However, mutations in other VCP residues are reported to be commonly associated with late-onset multisystem proteinopathy, for example, inclusion body myopathy with early-onset Paget disease and frontotemporal dementia (IBMPFD), and amyotrophic lateral sclerosis [18, 59].

In cancer patients, Plk1 was overexpressed in many types of tumor tissues when compared with the corresponding normal tissues; for example, the Log<sub>2</sub>FC was 1.333 and *p* value was less than 0.001 in lung cancer patients (Fig. S9H). Thus, we investigated whether the phosphorylation of Thr76 in VCP is a prominent feature in cancer tissues by performing phospho-VCP (T76) immunohistochemistry in lung cancer patient specimens. A total of 50 lung cancer patients' samples were examined, such that there were 17 patients with squamous cell carcinoma, 31 patients with adenocarcinoma and 2 patients with small cell lung cancer (Table S2). We demonstrated that the pT76-VCP signal in the

tumor tissues was 1.5-fold stronger than that in normal tissues ( $p < 0.0001$ ) (Fig. 7I). We also found that the pT76-VCP signal increased with the age of patients (Fig. S9I) but showed no correlation with the patient gender, TNM stage or metastasis conditions of the cancer (Table S2). In contrast, the expression level of VCP in cancer patients did not differ much between the tumor and normal tissues; for example, its Log<sub>2</sub>FC was  $-0.054$  and the *p* value was 0.056 in lung cancer patients (Fig. S9J). These data suggest that the phosphorylation level of Thr76 in VCP might be an indicator for cancer diagnosis.

## DISCUSSION

VCP mainly acts as a segregase to extract ubiquitinated proteins from complexes or membranes for degradation. VCP is also involved in membrane fusion events in the endomembrane system, playing a role in the reformation of the Golgi, ER, and nuclear envelope after mitosis. Here, we found that VCP interacts



with Eg5 (Fig. 4A, B). However, the level of Eg5 in VCP<sup>T76A</sup>-reconstituted cells was no different from that in control cells (Fig. 4B). The levels of total cellular ubiquitination or CHOP (an ER stress marker) in the VCP<sup>T76A</sup>-reconstituted cells were also similar to that in the VCP<sup>WT</sup>-reconstituted cells (Fig. S5E–G). These data

suggest that VCP does not act as a segregase to extract Eg5 for degradation. Instead, the phosphorylation of Thr76 in VCP is important for the recruitment of Eg5 to the spindle (Figs. 4C–E and S4C), which suggests that VCP acts as a scaffold to assemble Eg5 to the spindle.

**Fig. 7 VCP T76A mutation suppresses tumor formation in xenograft mouse model.** **A** The knockdown of VCP with shRNA and the reconstitution of shRNA-resistant VCP<sup>WT</sup> or VCP<sup>T76A</sup> in MDA-MB-231 cells were assessed by VCP immunoblotting. **B–H** The VCP<sup>WT</sup> or VCP<sup>T76A</sup>-reconstituted MDA-MB-231 cells were subjected to 3D culture in Matrigel, the tumor spheroids number was quantified. Scale bar, 50  $\mu$ m (**B**). The VCP<sup>WT</sup> or VCP<sup>T76A</sup>-reconstituted MDA-MB-231 cells were implanted into nude mice, the tumor volume (**C**) and excised tumor mass (**D**) were measured, and the images of xenograft tumors were shown (**E**). The primary tumor isolated from nude mice implanted with VCP<sup>WT</sup>- or VCP<sup>T76A</sup>-reconstituted MDA-MB-231 cells were subjected to RNA-Seq analysis, gene set enrichment analysis (GSEA) on apoptosis genes were performed (NES = -1.38, Normalized  $p = 0.0255$ , FDR = 0.05) (**F**), and heat map of representative tumor-related genes was presented (**G**). Formalin fixed paraffin embedded tumor tissues isolated from nude mice implanted with VCP<sup>WT</sup>- or VCP<sup>T76A</sup>-reconstituted MDA-MB-231 cells were subjected to TUNEL assay. Scale bar, 100  $\mu$ m (**H**). **I** Representative images of phospho-VCP (T76) IHC staining of tumor tissue and normal tissue in lung cancer patients were shown and their relative p-VCP signals were quantified. Scale bar, 100  $\mu$ m. The blots, images, and graphs are representative data from at least three independent experiments. The difference between two groups was analyzed using two-tailed Student's  $t$  test,  $p < 0.05$  was considered statistically significant. \* $p < 0.05$ , \*\* $p < 0.01$ , \*\*\* $p < 0.001$ , \*\*\*\* $p < 0.0001$ .

The ATPase activity of VCP is indispensable for cell cycle progression, especially in mitosis. For example, VCP works with p37/p47 to regulate the centrosomal Aurora A level for spindle alignment. It also cooperates with Ufd1/Npl4 to remove Aurora B from chromatin to allow the nucleus formation [27, 30, 60]. Of note, Thr76 mutations did not affect the ATPase activity of full-length VCP proteins (Fig. S8A). Thr76 is located at the N-terminal domain of VCP, which is responsible for the interaction with its cofactors. It is also close to the D1 ATPase domain, which mediates the oligomerization of VCP. A comparison of the cryo-EM structures of both VCP<sup>T76A</sup> and VCP<sup>T76E</sup> revealed how residue Thr76 might affect VCP. In VCP<sup>T76E</sup>, the glutamate act as a phosphorylation mimetic, and forms a hydrogen bond with residue Arg83. This, in turn, strengthens the interaction between the N-domain and the D1-domain and eventually influences the inter-subunit interactions (Fig. 6B–E). Thus, the phosphorylation of Thr76 might promote the coordination of both intra- and inter-subunit movement which may increase conformation-dependent cofactor binding, whereas dephosphorylation of Thr76 might lead to reduced coordination of VCP protein and hence decreased cofactor binding. Through phosphorylation and dephosphorylation, as mimicked by T76A and T76E, respectively as the two extremes, the functions of VCP might be subtly adjusted to suit the corresponding signaling events.

VCP-Thr76 was phosphorylated by Plk1 at the centrosome, and the treatment of mitotic cells with a Plk1 inhibitor abolished the centrosome localization of VCP (Figs. 2A–G and S2K). In addition, VCP<sup>T76A</sup> was not localized at centrosome (Fig. 2D), but Plk1 was still found at the centrosome in VCP<sup>T76A</sup>-reconstituted cells (Fig. S2N). These results indicate that the phosphorylation of Thr76 in VCP by Plk1 is required for its centrosomal localization, but Plk1's centrosomal localization is independent of VCP. Plk1 normally binds to a phosphorylation site on the substrate via its PBD [32, 33], and intriguingly, although VCP contains two potential motifs for PBD docking, mutation of the potential sites, T14 or T613, in VCP to alanine did not abolish the interaction between Plk1 and VCP (Fig. S1I). Notably, Plk1's PBD also binds to its own kinase domain, and the binding sequence in the kinase domain is <sup>315</sup>PITCLTIIPPR<sup>325</sup> [61], which does not match the PBD's core binding motif and none of these sites are phosphorylated. Along this line, we showed the interaction between VCP-ND1(1-481) and the MBP-PLK1-PBD domain (367-603) in vitro by ITC assay (Fig. 1C). Alternatively, it has been proposed previously that Plk1's PBD might bind to a phosphorylated scaffold at specific subcellular structures, e.g., centrosome or kinetochores, thereby allowing its kinase domain to phosphorylate the substrates in close proximity to these structures [62]. Two potential Plk1 scaffolds are Cdc23/Cut23 of the anaphase promoting complex [63, 64], and Mklp1/2, a kinesin-like protein [65, 66]. Therefore, it is also possible that Plk1 might use a phosphorylated scaffold at centrosome to phosphorylate VCP, although we showed the direct interaction between Plk1 and VCP in vitro (Fig. 1C).

VCP was not found at the spindle in VCP<sup>T76A</sup> or VCP<sup>T76E</sup>-reconstituted cells (Figs. 4G and S5A and S6B), and PTEN knockdown abolished the spindle localization of VCP as well (Figs. 5B and S7B). These data indicate that the dephosphorylation of VCP-Thr76 is required for the recruitment of VCP from the centrosome to the spindle. Regarding the cellular location where the phosphorylated Thr76 in VCP is dephosphorylated by PTEN, one possibility is that PTEN is only active in the spindle, although reports indicate that it is expressed at both the centrosome and spindle [15, 67]. If this is the case, then pVCP-T76 should be dephosphorylated by PTEN only after it relocates to the spindle. It is also possible that VCP is continuously phosphorylated by Plk1 at the centrosome during M phase, and pVCP-T76 is then dephosphorylated at the centrosome and/or spindle by PTEN during its recruitment from the centrosome to the spindle. This second possibility is supported by our finding that PTEN knockdown significantly increased the pVCP-T76 signals at the centrosome (Fig. 5C), and that VCP was enriched at the centrosome in the VCP<sup>T76E</sup>-reconstituted cells (Fig. S6B). We speculate that the phosphorylation and dephosphorylation switch of Thr76 enables VCP to recruit or remodel different substrates for centrosome movement or spindle orientation. Indeed, we identified several centrosome- or spindle-associated proteins in the BiOLD-VCP complex (Fig. S4A, B). It is of interest to assess whether these proteins interact with the phosphorylated or non-phosphorylated form of VCP. If they do, then the mechanism underlying how VCP regulates or remodels these proteins for centrosome or spindle architecture can be determined.

In addition to being a phospholipid phosphatase, PTEN can dephosphorylate polypeptides phosphorylated on Tyr, Ser, and Thr in vitro [47, 68]. It has also been reported to be able to dephosphorylate itself [47, 68] and various other protein substrates, such as focal adhesion kinase [69]; cyclic AMP response element-binding protein [70]; nonreceptor tyrosine kinase c-SRC [71]; insulin receptor substrate-1 [72]; and Eg5 [15], during a variety of physiologic or pathologic events. In addition, PTEN was found to act as a scaffold to load phosphorylated Eg5 (mediated by Nek9-Nek6 and Cdk1), to the centrosome via Dlg1, thereby controlling proper centrosome movement and bipolar spindle formation [16]. Here, we found that PTEN interacted with VCP (Fig. 5E) and was able to dephosphorylate the Thr76 in VCP in vitro (Fig. 5D). PTEN knockdown or deficiency abolished the localization of unphosphorylated VCP onto the spindle (Figs. 5B and S7B, D), and markedly increased the phosphorylation of Thr76 VCP signals at the centrosome (Fig. 5C). Remarkably, the mitotic defects in VCP<sup>T76E</sup>-expressing cells were similar to those observed in PTEN knockdown cells, e.g., a fragmented spindle pole and catastrophic mitotic failure (Fig. S6) [15, 16]. These data indicate that the dephosphorylation of Thr76 in VCP by PTEN is essential for faithful chromosome segregation. Although PTEN might act as a scaffold to dock another protein serine/threonine phosphatase to dephosphorylate VCP, this possibility is low given that knockdown of protein phosphatases such as PP1, PP2A, PP4, and PP6, or

treatment of mitotic cells with okadaic acid, a pan-PP1 and PP2A inhibitor, failed to affect the localization of VCP to the spindle (Fig. S7B, C).

Although the aneuploidy that results from chromosome instability generally results in tumorigenesis, recent studies have indicated that aneuploidy can either promote or inhibit tumorigenesis depending on the cell type, genomic context, cellular microenvironment, tumor stage, and immune system [73–75]. Here, we found that the VCP<sup>T76A</sup> mutation resulted in abnormal chromosome segregation due to defects in centrosome and spindle orientation (Fig. 3); however, the tumor growth in nude mice implanted with VCP<sup>T76A</sup>-reconstituted cancer cells was significantly slower when compared with those implanted with VCP<sup>WT</sup>-reconstituted cancer cells (Fig. 7C–E). RNA-seq analysis performed in tumor tissue harboring the VCP<sup>WT</sup> or VCP<sup>T76A</sup> mutation showed that DEGs were in a cell death cluster and a microenvironment cluster (Fig. 7F, G). For example, many genes related to cell death were upregulated in tumors harboring the VCP<sup>T76A</sup> mutation, and TUNEL assay confirmed that more cells in the VCP<sup>T76A</sup>-expressing tumor tissues were apoptotic, when compared with the VCP<sup>WT</sup>-expressing tumor tissues (Fig. 7H). Yet, the role of VCP<sup>T76A</sup> mutation in tumorigenesis needs to be further examined in cancer transgenic mouse models in the background of VCP<sup>T76A</sup> mutation.

In summary, we have mechanistically studied the role of VCP during the progression of the M phase. We demonstrated that Plk1 phosphorylates Thr76 in VCP at the centrosome during the M phase, and PTEN dephosphorylates Thr76. This dephosphorylation is a prerequisite for the enrichment of VCP and Eg5 at the spindle. We propose that VCP is first phosphorylated by Plk1 at the centrosome, and that pVCP-T76 is then dephosphorylated by PTEN during its recruitment to the spindle. This phosphorylation-dephosphorylation switch continues to occur during mitosis, and p-VCP can be continuously detected at the centrosome as long as Plk1 is there. This spatially and temporally regulated dynamic phosphorylation and dephosphorylation switch of VCP-Thr76 participates in the orientation of centrosome and spindle to enable the faithful segregation of chromosomes and hence helps maintain genome stability.

## MATERIALS AND METHODS

### Cell culture

HeLa cells, HEK 293T cells, MCF-7 cells, SK-OV-3 cells, MDA-MB-231 cells (ATCC) were maintained in Dulbecco's Modified Eagle Medium (DMEM) with 10% fetal bovine serum (FBS) and 1% penicillin-streptomycin in a 37 °C incubator with 5% CO<sub>2</sub>. Cells were passaged every 2–3 days. The HeLa, MCF-7 and MDA-MB-231 cells were verified by STR profiling.

### Antibodies and reagents

VCP antibody (#sc-133125), VCP antibody (#sc-374055), normal mouse IgG (#sc-2025), CHOP antibody (#sc-7351), HSP 70 antibody (#sc-24), PTEN antibody (#sc-7974), Mad 2 antibody (#sc-374131) and Centrin-2 antibody (#sc-27793-R) were from Santa Cruz. Plk1 antibody (#627702) and phospho-Plk1 (Thr210) (#628902) antibody were from BioLegend. The  $\alpha$ -tubulin antibody (#T6074),  $\gamma$ -tubulin antibody (#T6557), HA antibody (#11867423001) and Flag antibody (#F1804) were from Sigma. Eg5 antibody (#TA301478) was from Origene. GAPDH antibody (#60004-1) was from ProteinTech. CHOP (L63F7) antibody (#2895) and NRF-1 antibody (#80525) were from Cell Signaling Technology. phospho-Plk1 (Thr210) antibody (#558400) was from BD Biosciences. Strep-Tactin®-HRP (#1509-0089) was from IBA Lifesciences. The custom phospho-VCP (Thr76) antibody was generated by Abmart Inc.

DBeQ (#506190), Noc (#M1404), thymidine (#T9250), (+)-S-Trityl-L-cysteine (#164739), aprotinin (#A1153), PMSF (#11359061001), polybrene (#H9268), Duolink PLA kit (#DUO92101), Ni Sepharose High Performance (#GE17-5268-01), Percoll (#GE17-5445-02) were from Sigma. Puromycin (#A1113803), pepstatin A (#78436), leupeptin (#78435) were from

Invitrogen. BI2536 (#755038-02-9) was from Santa Cruz. HOpic (#S8651), CB-5083 (#S8101), CFI-400945 (#S7552), Alisertib (#S1133) and Barasertib (#S1147) were from Selleckchem. Okadaic acid (#5934) was from Cell Signaling Technology. Strep-Tactin® Sepharose® (#2-1201-010) was from IBA Lifesciences. Anti-Flag magnetic beads (B26101), Anti-HA magnetic beads (#B26201), Protein A/G Magnetic Beads (#B23202) and phosphatase inhibitors cocktail (#B15001) were from Bimake. The mRNA extraction kit (#220010) was from Fastagen. PrimeScript™ RT reagent Kit with gDNA Eraser (#RR047B) was from TAKARA. PEI (#689191) was from Shanghai Maokang.

### Molecular cloning

To knock down VCP, one 21 bp oligo based on human VCP gene (Table S3) was cloned into the pLKO.1 (addgene, #10878) by following protocols from addgene.

To knock out PTEN, two pairs of optimal sgRNA oligo were selected for human PTEN gene (Table S3). These sequences were then cloned into the lentiCRISPRv2 puro vector (addgene, #98290) by following protocols from addgene.

pENTR-His6-Flag vector was constructed by replacing GFP with His6-Flag in pENTR4-GFP-C1 vector (addgene, #17396). VCP cDNA resistant to its shRNA was mutated with QuikChange™ Site-Directed Mutagenesis Kit and it was then cloned into pENTR-His6-Flag vector to obtain the pENTR-His6-Flag-VCP<sup>WT</sup>. VCP<sup>T76A</sup> and VCP<sup>T76E</sup> were then mutated based on pENTR-His6-Flag-VCP<sup>WT</sup>. VCP<sup>WT</sup>, VCP<sup>T76A</sup> or VCP<sup>T76E</sup> in pENTR vector was finally exchanged into plenti-CMV-Puro-DEST (addgene, #17452) using Gateway LR reaction (Invitrogen).

VCP<sup>WT</sup> was also cloned into pBiFC-VN173 (addgene, #22010), while Plk1 was cloned into pBiFC-VC155 (addgene, #22011) to study the interactions between VCP and Plk1 during M phase. Twin-Strep-VCP, Twin-Strep-Plk1, or Twin-Strep-Eg5 was cloned into pcDNA3.1(+) vector.

### Cell synchronization

HeLa cells were synchronized to G1/S boundary using DTB method. Briefly, HeLa cells were grown to about 40% confluence and then incubated with thymidine (2 mM) for 19 h. Thereafter, thymidine was released by PBS washing for three times; and cells were then incubated with fresh medium without thymidine for 9 h. Thymidine (2 mM) was added back for another 16 h incubation to synchronize cells at G1/S boundary. Finally, cells were washed with PBS for three times and incubated in fresh medium to progress through the cell cycle.

Cells were also synchronized to prometaphase by overnight (around 16 h) treatment with Noc (50 ng/ml) and collected with mitotic shake-off.

### Lentivirus production and infection

The lentivirus production and infection were performed as described previously [76].

### Western blot analysis and immunoprecipitation (IP)

Western blot analysis and immunoprecipitation (IP) were performed as described previously [77]. The lysis buffer for endogenous IP is 50 mM Tris, 150 mM NaCl, 0.5% Tween 20, pH 7.5. Lysates were incubated with primary antibody or mouse IgG for overnight at 4 °C and collected for protein A/G beads binding for 2 h at room temperature. The beads were washed with lysis buffer for three times and subjected to western blot analysis.

### Transient transfection

The plasmids or siRNAs were transiently transfected into HeLa cells or HEK293T cells as described previously [77].

### mRNA extraction and RT-qPCR

mRNA extraction and RT-qPCR were performed as described previously [77].

### 3D culture

3D cultures were prepared as previously described [78]. Briefly, Flag-VCP<sup>WT</sup>- and Flag-VCP<sup>T76A</sup>-expressing MDA-MB-231 cells were seeded in 96-well plate with DMEM medium containing 10% FBS and 2% Matrigel. Assay medium (~100  $\mu$ l) was added every 4 days. The number of spheroids was quantified.

### PI staining and FACS analysis

HeLa cells were first synchronized to G1/S boundary with DTB in 6-well plates, thymidine was then released, and cells were collected every 2 h until 14 h after release. These cells were fixed in 70% ethanol for 30 min on ice and stored in 70% ethanol overnight at  $-20^{\circ}\text{C}$ . On the next day, cells were collected by centrifugation, washed with PBS, and subjected to PI staining (20 mg/ml PI, 0.1 mg/ml RNase A, 0.05% Triton X-100 in PBS) for 20 min in dark at room temperature. Thereafter, cells were washed with PBS and re-suspended with PBS. These cells were then filtered with 0.4  $\mu\text{m}$  cell filters and analyzed by FACS Canto II analytic flow cytometer. Data were analyzed by FlowJo software.

### Imaging

For live-cell imaging, HeLa cells infected with H2B-RFP lentivirus were plated on 6-well plates and synchronized to G1/S boundary by DTB. In total, 7 h after second thymidine release, cells were subjected to live imaging. The images were captured every 10 min with  $\times 40$  objectives of Carl Zeiss LSM 510 Meta inverted microscope equipped with Cy3/EGFP/DAPI filters. Data were analyzed with ImageJ software. The VCP<sup>WT</sup>, VCP<sup>T76A</sup>, and VCP<sup>T76E</sup>-reconstituted cells were imaged and quantified all together in repeated experiments but presented separately in Figs. 3A–C and S6G–I.

For fixed cell imaging, cells grown on coverslips were firstly synchronized to mitosis with DTB release, fixed with 4% PFA in PBS for 20 min at room temperature, washed with PBS, and then either fixed in  $-20^{\circ}\text{C}$  with cold 100% methanol for 15 min or not. These cells were then blocked with 1% normal goat serum and 1% BSA in PBST (PBS + 0.1% Triton) for 1 h at room temperature. Cells were incubated with primary antibody at room temperature for 2 h, or overnight at  $4^{\circ}\text{C}$ , or at  $37^{\circ}\text{C}$  for 0.5 h. After washing with PBST, cells were incubated with secondary antibody for 1 h at room temperature. After washing with PBST, cells were subjected to nuclei staining with DAPI (0.5 g/ml) for 5 min at room temperature. Finally, cells were mounted with Prolong Gold Antifade Reagent on slides. Images were taken by Carl Zeiss LSM 880 confocal microscope or Nikon A1HD25 High speed and Large Field of View Confocal Microscope using  $\times 63$  oil objective and analyzed by ZEN software or Nikon offline software. For the angle of centrosomes, it was imaged with Carl Zeiss LSM 880 and analyzed with software ICY. Super-resolution SIM images were taken by Nikon N-SIM and analyzed by Nikon offline software.

### Image analysis

The Manders' colocalization coefficients (MCC) evaluation of VCP, p-VCP, Eg5, or Venus-Plk1/VCP over  $\gamma$ -tubulin or  $\alpha$ -tubulin was performed by Coloc 2 Plug-in in ImageJ software. In MCC, two MCC values (M1 and M2) are calculated for two probes, e.g., R and G. M1 represents the fraction of R (e.g.,  $\gamma$ -tubulin in our analysis) colocalized with G (e.g., VCP in our analysis) in total R, and M2, the fraction of G colocalized with R in total G. For example, we used M1 to represent the percentage of  $\gamma$ -tubulin colocalized with VCP or p-VCP in total  $\gamma$ -tubulin. In general, MCC methods based on the workflow described by Dunn et al. were performed on single plane images [79].

Eg5 at the mitotic spindle was quantified in ImageJ as the following steps: the spindle area was first selected with an ROI, and the same ROI was applied to Eg5 to measure the intensity of  $\alpha$ -tubulin and Eg5. The abundance of Eg5 was finally normalized with  $\alpha$ -tubulin intensity.

### In vitro kinase assay and in vitro phosphatase assay

For Plk1 in vitro kinase assay, Twin-Strep-Plk1 was transfected into HEK293T cells. Cells were then synchronized to M phase by incubation with Noc (50 ng/ml). The cells were lysed and Twin-Strep-Plk1 was pulled down with Strep-Tactin<sup>®</sup> Sepharose<sup>®</sup> and washed three times with 1 M NaCl + 0.5% CA630. The beads were washed once with the in vitro kinase buffer and subjected to an in vitro kinase assay. Recombinant VCP<sup>WT</sup> and VCP<sup>T76A</sup> proteins were purified from bacterial culture. Twin-Strep-Plk1 beads were incubated with VCPWT or VCP<sup>T76A</sup> proteins in the kinase assay buffer (20 mM Hepes-KOH, pH 7.7, 50 mM sucrose, 100 mM KCl, 5 mM MgCl<sub>2</sub>, 0.5 mM EGTA, 1 mM DTT, 0.05% Tween 20, 0.1 mg/ml BSA, and 1 mM ATP) at room temperature for 1 h. The reaction was stopped by adding 2x SDS buffer and subjected to western blot analysis.

For the in vitro phosphatase assay of PTEN, HA-PTEN-expressing HEK 293T cells were treated with Noc (50 ng/ml) and HA-PTEN was purified with HA beads. The HA-PTEN beads were then washed with phosphatase washing buffer (20 mM HEPES, pH 7.2, 1 mM DTT, 1 mM MgCl<sub>2</sub>, 0.1 mg/ml BSA and 1 mM EDTA with protease inhibitors). Also, recombinant VCP

protein was phosphorylated by Twin-Strep-Plk1 in aforementioned in vitro kinase assay. The supernatant (phosphorylated VCP) were collected and Twin-Strep-Plk1 beads were removed by centrifugation. Afterward, HA-PTEN beads were incubated with phosphorylated VCP in phosphatase reaction buffer (50 mM Tris, pH 7.5, 100 mM NaCl, 10 mM MgCl<sub>2</sub>, 1% glycerol, and 10 mM DTT) at  $30^{\circ}\text{C}$  for 1 h. The reaction was stopped by adding 2x SDS buffer and subjected to western blot analysis.

### Duolink<sup>®</sup> proximity ligation assay (PLA) technology

HeLa cells plated on coverglass were synchronized to M phase with DTB release. Duolink<sup>®</sup> PLA assay was conducted according to the manufacturer's protocol. Briefly, the cells were firstly fixed with 4% PFA followed by methanol incubation. Cells on coverglass were then fixed with Duolink<sup>®</sup> Blocking Solution in a heated humidity chamber at  $37^{\circ}\text{C}$  for 60 min. After blocking, cells were incubated with primary antibody which was diluted in the Duolink<sup>®</sup> Antibody Diluent at  $4^{\circ}\text{C}$  for overnight. VCP or Plk1 antibodies were 1:100 diluted, while  $\alpha$ -tubulin antibody was 1:1000 diluted for the assay. Afterwards, cells were washed with wash buffer A twice at room temperature for 5 min, and were then incubated with Duolink<sup>®</sup> PLA Probe for 1 h at  $37^{\circ}\text{C}$ . After PLA probe incubation, cells were again washed with wash buffer A twice at room temperature for 5 min followed by 30 min incubation with Duolink<sup>®</sup> Ligation buffer at  $37^{\circ}\text{C}$ . Thereafter, cells were washed again with wash buffer A twice at room temperature for 5 min and incubated with polymerase in amplification buffer at  $37^{\circ}\text{C}$  for 100 min. After polymerization, cells were finally washed with wash buffer B twice for 10 min and 0.01x wash buffer B for 1 min followed by DAPI staining for confocal imaging.

### Bimolecular fluorescence complementation (BiFC)

During the DTB synchronization, 0.25  $\mu\text{g}$  pBiFC-VN173-VCP and pBiFC-VC155-Plk1 plasmid were co-transfected into HeLa cells in 24 well plates by lipofectamine 2000. Cells at mitosis were collected and co-stained with centrosome marker  $\gamma$ -tubulin for further confocal image analysis.

### Protein expression and purification

VCP<sup>WT</sup>, VCP<sup>T76A</sup>, and VCP<sup>T76E</sup> were fused with a MBP tag and constructed into pET28a plasmid by restriction enzyme cloning. Plk1-PBD (367-603) was also fused with a MBP tag and constructed into a pRSET backbone. All proteins were expressed in SHuffle T7 E. coli Cells (C3026 New England Biolabs) by induction with IPTG (0.3 mM) at 0.8 of OD600 and subsequent overnight incubation at  $20^{\circ}\text{C}$ . Cells were re-suspended in Ni<sup>2+</sup> column buffer A (25 mM HEPES, pH 7.5, 300 mM KCl, 5 mM MgCl<sub>2</sub>, 5% Glycerol, 0.03%  $\beta$ -ME), lysed by nano homogenize machine (AH-NANO ATS Engineering Limited) and purified by HisTrap HP purification columns (GE Healthcare). After protein elution with Ni column buffer B (25 mM HEPES, pH7.5, 300 mM KCl, 5 mM MgCl<sub>2</sub>, 500 mM Imidazole, 5% Glycerol, 0.03%  $\beta$ -ME), proteins were further purified with MBPTrap HP column (GE Healthcare) and dialyzed against TEV digestion buffer (50 mM Tris-HCl, pH7.5, 150 mM NaCl, 5 mM MgCl<sub>2</sub>, 5 mM Sodium Citrate, 5% Glycerol, 0.03%  $\beta$ -ME). MBP tag was then cleaved by TEV protease overnight at  $4^{\circ}\text{C}$  and removed by Ni<sup>2+</sup> HisTrap HP column. Proteins were concentrated and re-diluted into gel filtration buffer (25 mM HEPES, pH7.5, 300 mM KCl, 5 mM MgCl<sub>2</sub>, 0.01%  $\beta$ -ME) before removal of prebound ADP by overnight Apyrase digestion at  $4^{\circ}\text{C}$ , followed by gel filtration as the final purification step. During gel filtration process, only protein fractions corresponding to hexamers were collected. Protein samples were finally concentrated to 20 mg/ml, flash-frozen by liquid nitrogen, and stored at  $-80^{\circ}\text{C}$ .

### Animal study

NSG mice was purchased from the Jackson Laboratory (USA) and maintained in pathogen-free conditions with a 12 h light/dark cycle. All animal studies were performed according to the guidelines approved by the Animal Ethics Committee of City University of Hong Kong. For xenograft experiments, female mice at 6-weeks-old were selected. A total of ten mice were randomly and equally divided into two experimental groups. Ten million Flag-VCP<sup>WT</sup>- or Flag-VCP<sup>T76A</sup>-expressing MDA-MB-231 cells were diluted in 100  $\mu\text{l}$  PBS mixed with an equal volume of Matrigel (BD Biosciences) and inoculated via subcutaneous route into the flank of NSG mice. Once palpable tumors were established, the tumor volumes were measured every 5 days. Tumor weight was measured at the end of the experiment. Investigators were blinded when conducting the animal experiments.

## RNA sequencing

The tumors derived from Flag-VCP<sup>WT</sup>- or Flag-VCP<sup>T76A</sup>-expressing MDA-MB-231 cells ( $n=3$ ) were collected for sequencing according to the standard protocol. Briefly, total RNA of each sample was extracted using TRIzol Reagent (Invitrogen)/RNeasy Mini Kit (Qiagen). Total RNA of each sample was quantified and qualified by Agilent 2100 Bioanalyzer (Agilent Technologies, Palo Alto, CA, USA), NanoDrop (Thermo Fisher Scientific Inc.), or 1% agarose gel. Total RNA (1  $\mu$ g) with RIN value above 6.5 was used for library preparation. Next-generation sequencing library preparations were constructed according to the manufacturer's protocol. The poly(A) mRNA isolation was performed using Poly(A) mRNA Magnetic Isolation Module or rRNA removal Kit. The mRNA fragmentation and priming were performed using First-Strand Synthesis Reaction Buffer and Random Primers. First-strand cDNA was synthesized using ProtoScript II Reverse Transcriptase and the second-strand cDNA was synthesized using Second-Strand Synthesis Enzyme Mix. The purified double-stranded cDNA by beads was then treated with End Prep Enzyme Mix to repair both ends and add a dA-tailing in one reaction, followed by a T-A ligation to add adapters to both ends. Size selection of adapter-ligated DNA was then performed using beads, and fragments of ~420 bp (with the approximate insert size of 300 bp) were recovered. Each sample was then amplified by PCR for 13 cycles using P5 and P7 primers, with both primers carrying sequences which can anneal with flow cells to perform bridge PCR and P7 primer carrying a six-base index allowing for multiplexing. The PCR products were cleaned up using beads, validated using a Qsep100 (Bioptic, Taiwan, China), and quantified by Qubit3.0 Fluorometer (Invitrogen, Carlsbad, CA, USA). Then libraries with different indices were multiplexed and loaded on an Illumina HiSeq instrument according to manufacturer's instructions (Illumina, San Diego, CA, USA). Sequencing was carried out using a 2  $\times$  150 bp paired-end configuration; image analysis and base calling were conducted by the Novaseq Control Software RTA3 on the Illumina NovaSeq 6000 instrument. The sequences were processed and analyzed by GENEWIZ. For the mapping, reference genome sequences and gene model annotation files of relative species were firstly downloaded from the genome website, such as UCSC, NCBI, ENSEMBL. Secondly, Hisat2 (v2.0.1) was used to index the reference genome sequence. Finally, clean data were aligned to the reference genome via software Hisat2 (v2.0.1). For the expression analysis, transcripts in fasta format were converted from known gff annotation files and indexed properly. Then, with the file as a reference gene file, HTSeq (v0.6.1) estimated gene and isoform expression levels from the pair-end clean data. Differential expression analysis was performed by using the DESeq2 Bioconductor package, a model based on the negative binomial distribution. The estimates of dispersion and logarithmic fold changes incorporate data-driven prior distributions, and  $P_{adj}$  of genes were set <0.1 to detect differential expressed ones. The RNA sequences have been deposited into GEO with accessing codes of GSE147636.

## TUNEL assay

TUNEL assay was performed with the DeadEnd™ Fluorometric TUNEL kit (Promega) following the manufacturer's protocol. Briefly, paraffin-embedded tumor tissue sections were washed twice in xylene for 5 min to remove paraffin. The sections were immersed in 100% ethanol for 5 min and then washed in decreasing concentrations of ethanol (100, 95, 70, and 50%), 5 min for each wash. After that, the section was washed with PBS for 5 min. The sections were then fixed with 4% PFA in PBS for 15 min and washed twice with PBS. The sections were incubated with proteinase K solution (20  $\mu$ g/ml) for 10 min and then washed once with PBS. The sections were fixed again with 4% PFA and washed with PBS, and incubated with equilibration buffer (~100  $\mu$ l). Following the equilibration, the sections were labeled with TdT reaction mix (~50  $\mu$ l) at 37 °C for 1 h and the reaction was stopped with incubation in 2x SSC buffer for 15 min. The sections were washed with PBS and stained with DAPI, and the green fluorescence of apoptotic tissue was detected under microscope.

## Immunohistochemistry for patient sample

Pathological sections of lung cancer patients were obtained from the Pathology Department of the Second Affiliated Hospital of Chongqing Medical University, with informed consent and approval from the Clinical Research Ethics Committee of the Second Affiliated Hospital of Chongqing Medical University. The patients were provided and signed the consent forms. Tumor sections were incubated with the antibodies against phospho-VCP (Thr76) overnight at 4 °C. The remaining steps were performed using the Immunohistochemistry kit. The relative intensity of IHC sample was quantified with the image-pro plus software.

## ATPase activity determination

ATPase activity was detected by measuring inorganic phosphate released during ATP hydrolysis, which reacts with a complex of molybdate and malachite green. A total amount of 10  $\mu$ g protein was added into 50  $\mu$ l assay buffer (50 mM Tris-HCl, pH 8.0, 20 mM MgCl<sub>2</sub>, 1 mM EDTA, 1 mM DTT and 4 mM ATP) and incubated at 37 °C for 10 min. In total, 800  $\mu$ l dye buffer (A fresh mix of 0.045% malachite green in a 1:3 ratio with 1.4% ammonium molybdate tetrahydrate in 4 N HCl) was added to the reaction solution to stop the reaction, followed by addition of 100  $\mu$ l 34% sodium citrate. After another 10 min incubation at room temperature, 16  $\mu$ l 10% Tween-20 was added to the solution and mixed by pipetting. Absorbance was measured at 660 nm on VARIOSKAN LUX (Thermo Scientific). Further calculation was performed with the system software.

## Determination of binding affinity between Plk1 and VCP by ITC

ITC experiments were carried out using MicroCal PEAQ-ITC. Protein samples were dialyzed against ITC Buffer (20 mM Tris, PH8.0, 50 mM NaCl) and filtered by 0.22  $\mu$ m syringe filter (MiliQ). The experiment was performed by titrating 300  $\mu$ l of 50 mM MBP-PBD protein or MBP protein with 60  $\mu$ l of 500 mM VCP-WT-ND1 protein. All titration assays were performed at 25 °C and the binding affinity was calculated by system-integrated software.

## EM specimen preparation and data collection

Sample homogeneity was first determined by negative staining with 2% uranyl Acetate. The negative staining samples were examined with 120 kV FEI Talos TEM machine (Thermo Fisher Scientific) in the Cryo-EM center at Southern University of Science and Technology, with a nominal magnification around  $\times 50,000$ .

To prepare cryo-EM specimens, protein samples were diluted with sample buffer (25 mM HEPES, 50 mM NaCl, 5 mM MgCl<sub>2</sub>, 0.01%  $\beta$ -ME, PH7.5), and then concentrated to 2 mg/ml for grid preparation. ATP analog AMP-PNP and ADP were added to samples 30 min before grid preparation. In total, 3  $\mu$ l of prepared samples were applied to glow-discharged M004-Cu300-R1.2/1.3 Copper grid (CryoMatrix) and blotted for 2.5 s in FEI Vitrobot (Thermo Fisher Scientific). Samples were frozen by liquid ethane after blotting and stored in liquid nitrogen.

The samples were examined in the Cryo-EM center at Southern University of Science and Technology. Grids were imaged on Titan Krios G3 (Thermo Fisher Scientific) with FEI Falcon 3 detector. Images were recorded at a nominal magnification of  $\times 96,000$ , corresponding to a calibrated pixel size of 1.073 Å. For each image, 39 frames were recorded with an accumulative doze of 60 e<sup>-</sup>/Å<sup>2</sup>.

## Image processing

Motion correction and CTF find were performed with Relion 3.0.6. Each picture was manually inspected and selected based on image quality, after which, around 1000 particles were manually picked for each dataset as templates of autopicking process.

For VCP<sup>T76A</sup> + ADP dataset, 528,526 particles were autopicked and extracted from 2724 pictures. The particle stack was then subjected to 20 rounds of 2D classification and 222,628 particles were selected and re-extracted thereafter. The initial model was produced by CisTEM beta-1.0.0. The particle stack was subject to 20 rounds of 3D classification and one class with highest estimated resolution (53,858 particles) was selected and subjected to 3D refinement. Final resolution of density map is 3.9 Å.

For VCP<sup>T76E</sup> + ADP dataset, 562,693 particles were autopicked and extracted from 1993 pictures. After 20 rounds of 2D classification, 273,610 particles were selected and re-extracted. Initial model was produced by CisTEM beta-1.0.0. Particles were subjected to 25 rounds of 3D classification and 243,820 particles were selected based on 3D classification results. A 3.6 Å final map is generated based on this final particle stack.

For VCP<sup>T76A</sup> + AMP-PNP dataset, around 2.2 M particles were autopicked from 2451 pictures and extracted with a boxsize of 360  $\times$  360 pixels. The particles were then subjected to 25 rounds of 2D Classification, 1,524,038 particles were selected and re-extracted. Extracted particle stack was then imported into CisTEM beta-1.0.0. Initial model was generated by Ab-Initio module of CisTem, 20 rounds of global 3D refinement was carried out using 6 classes. Three classes were discarded because of low occupation and poor resolution. The three remaining classes – Class1 (291,035 particles), Class2 (532,334 particles) and Class3 (701,131 particles) were then subjected to auto-refine procedure. The outlines of Class1 and



Class2 showed better resolution around the N-domain and corresponded to the “Down” and “Up” forms, respectively. Class3 showed relatively low-resolution around the N-domain. Class1 and Class2 were further re-extracted and subclassed. A 3.3 Å final density map for Class1 was obtained with a subclass of 229,297 particles. Final resolution for Class2 density map was around 4.1 Å with a final particle stack of 354,977 particles.

For VCP<sup>T76E</sup> + AMP-PNP dataset, around 2.1 M particles were autopicked from 2531 pictures. Particles were extracted with boxes of 360 × 360 pixels size. The particle stack was subjected to 25 rounds of 2D Classification, after which 1,650,009 particles were selected and re-extracted. Extracted particle stack was then imported into CisTEM beta-1.0.0. Initial model was generated by Ab-Initio module, and 25 rounds of global 3D refinement were carried out using 8 classes. Six classes were eliminated from the project due to low occupation and poor resolution. Only two major classes with high occupation were retained: Class1 (474,530 particles) and Class2 (727,253 particles). These two classes were further processed by autorefine module. Class1 showed density corresponding to the “Down” form and density map for class2 corresponded to the “Up” form. However, the density for the N-domain region was very obscure in both classes. Class1 was further classified into two subclasses of 229,297 particles and 245,233 particles. The first subclass showed better rigidity for N-domain and was subjected for construction of final map of 4.2 Å resolution. Class 2 was also further processed by two rounds of sub-classification and ended up with a final map of 4.8 Å resolution generated from 533,495 particles.

### Model building and refinement

The structures of human VCP protein (PDB ID: 5ftl; 5ftn; 5dyg; 6g2z; 5dyg; 3hu1) were used as initial models for model building and model templates for refinement. The initial model of VCP single subunit was produced in COOT 0.9 and nucleotides were fitted into the binding pockets of D1 and D2 domains. Initial Model was docked into density maps using Dock in Map module of Phenix 1.16 and was then subjected to multiple rounds of Real-space refinement. Six-fold symmetry was maintained during refinement process and rigid body option was always selected for every refinement run. The final models were checked in COOT and verified with the Comprehensive Validation module of Phenix.

The coordinates and EM maps for VCP<sup>T76A</sup> + ADP, VCP<sup>T76A</sup> + AMP-PNP, VCP<sup>T76E</sup> + ADP and VCP<sup>T76E</sup> + AMP-PNP have been deposited into Protein Data Bank with accessing codes of 7BP8, 7BPA, 7BP9 and 7BPB, respectively.

### Statistical analysis

Sample sizes were determined based on the amount of data required to give the statistical significance ( $n \geq 3$ ). Significant differences between two groups were determined by unpaired Student's *t* test using GraphPad Prism 8.0 software. All statistical results were expressed as mean values ± SEM, and  $p < 0.05$  was considered statistically significant.

### DATA AVAILABILITY

Data supporting the present study are available from the corresponding author upon reasonable request.

### REFERENCES

- Tanenbaum ME, Medema RH. Mechanisms of centrosome separation and bipolar spindle assembly. *Dev Cell*. 2010;19:797–806.
- Nigg EA, Stearns T. The centrosome cycle: centriole biogenesis, duplication and inherent asymmetries. *Nat Cell Biol*. 2011;13:1154–60.
- Nilsson J. Protein phosphatases in the regulation of mitosis. *J Cell Biol*. 2019;218:395–409.
- Gelens L, Qian J, Bollen M, Saurin AT. The importance of kinase-phosphatase integration: lessons from mitosis. *Trends Cell Biol*. 2018;28:6–21.
- Dominguez-Brauer C, Thu KL, Mason JM, Blaser H, Bray MR, Mak TW. Targeting mitosis in cancer: emerging strategies. *Mol Cell*. 2015;60:524–36.
- Archambault V, Glover DM. Polo-like kinases: conservation and divergence in their functions and regulation. *Nat Rev Mol Cell Biol*. 2009;10:265–75.
- Combes G, Alharbi I, Braga LG, Elowe S. Playing polo during mitosis: PLK1 takes the lead. *Oncogene*. 2017;36:4819–27.
- Strebhardt K. Multifaceted polo-like kinases: drug targets and antitargets for cancer therapy. *Nat Rev Drug Disco*. 2010;9:643–60.

- Gutteridge REA, Ndiaye MA, Liu X, Ahmad N. Plk1 inhibitors in cancer therapy: from laboratory to clinics. *Mol Cancer Ther*. 2016;15:1427–35.
- Mann BJ, Wadsworth P. Kinesin-5 regulation and function in mitosis. *Trends Cell Biol*. 2019;29:66–79.
- Bertran MT, Sdelci S, Regue L, Avruch J, Caelles C, Roig J. Nek9 is a Plk1-activated kinase that controls early centrosome separation through Nek6/7 and Eg5. *EMBO J*. 2011;30:2634–47.
- Blangy A, Lane HA, d'Hérin P, Harper M, Kress M, Nigg EA. Phosphorylation by p34cdc2 regulates spindle association of human Eg5, a kinesin-related motor essential for bipolar spindle formation in vivo. *Cell*. 1995;83:1159–69.
- Sawin KE, Mitchison TJ. Mutations in the kinesin-like protein Eg5 disrupting localization to the mitotic spindle. *Proc Natl Acad Sci USA*. 1995;92:4289–93.
- Sawin KE, LeGuellac K, Philippe M, Mitchison TJ. Mitotic spindle organization by a plus-end-directed microtubule motor. *Nature*. 1992;359:540–3.
- He J, Zhang Z, Ouyang M, Yang F, Hao H, Lamb KL, et al. PTEN regulates EG5 to control spindle architecture and chromosome congression during mitosis. *Nat Commun*. 2016;7:12355.
- van Ree JH, Nam HJ, Jeganathan KB, Kanakkanthara A, van Deursen JM. Pten regulates spindle pole movement through Dlg1-mediated recruitment of Eg5 to centrosomes. *Nat Cell Biol*. 2016;18:814–21.
- Muretta JM, Reddy BJN, Scarabelli G, Thompson AF, Jariwala S, Major J, et al. A posttranslational modification of the mitotic kinesin Eg5 that enhances its mechanochemical coupling and alters its mitotic function. *Proc Natl Acad Sci USA*. 2018;115:E1779–88.
- van den Boom J, Meyer H. VCP/p97-mediated unfolding as a principle in protein homeostasis and signaling. *Mol Cell*. 2018;69:182–94.
- Stach L, Freemont PS. The AAA+ ATPase p97, a cellular multitool. *Biochem J*. 2017;474:2953–76.
- Bodnar N, Rapoport T. Toward an understanding of the Cdc48/p97 ATPase. *F1000Res*. 2017;6:1318.
- Deng L, Wu RA, Sonnevile R, Kochenova OV, Labib K, Pellman D, et al. Mitotic CDK promotes replisome disassembly, fork breakage, and complex DNA rearrangements. *Mol Cell*. 2019;73:915–29 e6.
- Franz A, Orth M, Pirson PA, Sonnevile R, Blow JJ, Gartner A, et al. CDC-48/p97 coordinates CDT-1 degradation with GINS chromatin dissociation to ensure faithful DNA replication. *Mol Cell*. 2011;44:85–96.
- Wu RA, Semlow DR, Kamimae-Lanning AN, Kochenova OV, Chistol G, Hodskinson MR, et al. TRAP1 is a master regulator of DNA interstrand crosslink repair. *Nature*. 2019;567:267–72.
- Shi X, Zhu K, Ye Z, Yue J. VCP/p97 targets the nuclear export and degradation of p27(Kip1) during G1 to S phase transition. *FASEB J*. 2020;34:5193–207.
- Raman M, Havens CG, Walter JC, Harper JW. A genome-wide screen identifies p97 as an essential regulator of DNA damage-dependent CDT1 destruction. *Mol Cell*. 2011;44:72–84.
- Meerang M, Ritz D, Paliwal S, Garajova Z, Bosshard M, Mailand N, et al. The ubiquitin-selective segregase VCP/p97 orchestrates the response to DNA double-strand breaks. *Nat Cell Biol*. 2011;13:1376–82.
- Ramadan K, Bruderer R, Spiga FM, Popp O, Baur T, Gotta M, et al. Cdc48/p97 promotes reformation of the nucleus by extracting the kinase Aurora B from chromatin. *Nature*. 2007;450:1258–62.
- Olmos Y, Hodgson L, Mantell J, Verkade P, Carlton JG. ESCRT-III controls nuclear envelope reformation. *Nature*. 2015;522:236–9.
- Cao K, Nakajima R, Meyer HH, Zheng Y. The AAA-ATPase Cdc48/p97 regulates spindle disassembly at the end of mitosis. *Cell*. 2003;115:355–67.
- Kress E, Schwager F, Holtackers R, Seiler J, Prodon F, Zanin E, et al. The UBXN-2/p37/p47 adaptors of CDC-48/p97 regulate mitosis by limiting the centrosomal recruitment of Aurora A. *J Cell Biol*. 2013;201:559–75.
- Yu CC, Yang JC, Chang YC, Chuang JG, Lin CW, Wu MS, et al. VCP phosphorylation-dependent interaction partners prevent apoptosis in *Helicobacter pylori*-infected gastric epithelial cells. *PLoS ONE*. 2013;8:e55724.
- Elia AE, Cantley LC, Yaffe MB. Proteomic screen finds pSer/pThr-binding domain localizing Plk1 to mitotic substrates. *Science*. 2003;299:1228–31.
- Elia AE, Rellos P, Haire LF, Chao JW, Ivins FJ, Hoepker K, et al. The molecular basis for phosphodependent substrate targeting and regulation of Plks by the Polo-box domain. *Cell*. 2003;115:83–95.
- Soderberg O, Gullberg M, Jarvius M, Ridderstrale K, Leuchowius KJ, Jarvius J, et al. Direct observation of individual endogenous protein complexes in situ by proximity ligation. *Nat Methods*. 2006;3:995–1000.
- Shyu YJ, Hiatt SM, Duren HM, Ellis RE, Kerppola TK, Hu CD. Visualization of protein interactions in living *Caenorhabditis elegans* using bimolecular fluorescence complementation analysis. *Nat Protoc*. 2008;3:588–96.
- Nakajima H, Toyoshima-Morimoto F, Taniguchi E, Nishida E. Identification of a consensus motif for Plk (Polo-like kinase) phosphorylation reveals Myt1 as a Plk1 substrate. *J Biol Chem*. 2003;278:25277–80.

37. Peters JM, Walsh MJ, Franke WW. An abundant and ubiquitous homo-oligomeric ring-shaped ATPase particle related to the putative vesicle fusion proteins Sec18p and NSF. *EMBO J*. 1990;9:1757–67.
38. Macůrek L, Lindqvist A, Lim D, Lampson MA, Klompaker R, Freire R, et al. Polo-like kinase-1 is activated by aurora A to promote checkpoint recovery. *Nature*. 2008;455:119–23.
39. Seki A, Coppinger JA, Jang C-Y, Yates JR, Fang G. Bora and the kinase Aurora a cooperatively activate the kinase Plk1 and control mitotic entry. *Science*. 2008;320:1655–8.
40. Lee K, Rhee K. PLK1 phosphorylation of pericentrin initiates centrosome maturation at the onset of mitosis. *J Cell Biol*. 2011;195:1093–101.
41. van Vugt MA, van de Weerd BC, Vader G, Janssen H, Calafat J, Klompaker R, et al. Polo-like kinase-1 is required for bipolar spindle formation but is dispensable for anaphase promoting complex/Cdc20 activation and initiation of cytokinesis. *J Biol Chem*. 2004;279:36841–54.
42. Liu X, Erikson RL. Activation of Cdc2/cyclin B and inhibition of centrosome amplification in cells depleted of Plk1 by siRNA. *Proc Natl Acad Sci USA*. 2002;99:8672–6.
43. Li Y, Benezra R. Identification of a human mitotic checkpoint gene: *hMAD2*. *Science*. 1996;274:246–8.
44. Kim DI, Jensen SC, Noble KA, Kc B, Roux KH, Motamedchaboki K, et al. An improved smaller biotin ligase for BioID proximity labeling. *Mol Biol Cell*. 2016;27:1188–96.
45. Anderson DJ, Le Moigne R, Djakovic S, Kumar B, Rice J, Wong S, et al. Targeting the AAA ATPase p97 as an approach to treat cancer through disruption of protein homeostasis. *Cancer Cell*. 2015;28:653–65.
46. Erdodi F, Rokolya A, Di Salvo J, Barany M, Barany K. Effect of okadaic acid on phosphorylation-dephosphorylation of myosin light chain in aortic smooth muscle homogenate. *Biochem Biophys Res Commun*. 1988;153:156–61.
47. Zhang XC, Piccini A, Myers MP, Van Aelst L, Tonks NK. Functional analysis of the protein phosphatase activity of PTEN. *Biochem J*. 2012;444:457–64.
48. Banerjee S, Bartesaghi A, Merk A, Rao P, Bulfer SL, Yan Y, et al. 2.3 Å resolution cryo-EM structure of human p97 and mechanism of allosteric inhibition. *Science*. 2016;351:871–5.
49. Tang WK, Li D, Li CC, Esser L, Dai R, Guo L, et al. A novel ATP-dependent conformation in p97 N-D1 fragment revealed by crystal structures of disease-related mutants. *EMBO J*. 2010;29:2217–29.
50. Tang WK, Xia D. Altered intersubunit communication is the molecular basis for functional defects of pathogenic p97 mutants. *J Biol Chem*. 2013;288:36624–35.
51. Liu-Chittenden Y, Jain M, Gaskins K, Wang S, Merino MJ, Kotian S, et al. RARRES2 functions as a tumor suppressor by promoting beta-catenin phosphorylation/degradation and inhibiting p38 phosphorylation in adrenocortical carcinoma. *Oncogene*. 2017;36:3541–52.
52. Kim JY, Xue K, Cao M, Wang Q, Liu JY, Leader A, et al. Chemerin suppresses ovarian follicular development and its potential involvement in follicular arrest in rats treated chronically with dihydrotestosterone. *Endocrinology*. 2013;154:2912–23.
53. Zhang H, Wang Y, Liu Z, Yao B, Dou C, Xu M, et al. Lymphocyte-specific protein 1 inhibits the growth of hepatocellular carcinoma by suppressing ERK1/2 phosphorylation. *FEBS Open Bio*. 2016;6:1227–37.
54. Irigoyen M, Pajares MJ, Agorreta J, Ponz-Sarvisse M, Salvo E, Lozano MD, et al. TGFB1 expression is associated with a better response to chemotherapy in NSCLC. *Mol Cancer*. 2010;9:130.
55. Smith CC, Lee KS, Li B, Laing JM, Hersl J, Shvartsbeyn M, et al. Restored expression of the atypical heat shock protein H11/HspB8 inhibits the growth of genetically diverse melanoma tumors through activation of novel TAK1-dependent death pathways. *Cell Death Dis*. 2012;3:e371.
56. Lewis AM, Varghese S, Xu H, Alexander HR. Interleukin-1 and cancer progression: the emerging role of interleukin-1 receptor antagonist as a novel therapeutic agent in cancer treatment. *J Transl Med*. 2006;4:48.
57. Alfaro C, Sanmamed MF, Rodríguez-Ruiz ME, Teijeira Á, Oñate C, González Á, et al. Interleukin-8 in cancer pathogenesis, treatment and follow-up. *Cancer Treat Rev*. 2017;60:24–31.
58. Masjedi A, Hashemi V, Hovjat-Farsangi M, Ghalamfarsa G, Azizi G, Yousefi M, et al. The significant role of interleukin-6 and its signaling pathway in the immunopathogenesis and treatment of breast cancer. *Biomed Pharmacother*. 2018;108:1415–24.
59. Kimonis VE, Fulchiero E, Vesa J, Watts G. VCP disease associated with myopathy, Paget disease of bone and frontotemporal dementia: review of a unique disorder. *Biochim Biophys Acta*. 2008;1782:744–8.
60. Dobrynin G, Popp O, Romer T, Bremer S, Schmitz MH, Gerlich DW, et al. Cdc48/p97-Ufd1-Npl4 antagonizes Aurora B during chromosome segregation in HeLa cells. *J Cell Sci*. 2011;124:1571–80.
61. Xu J, Shen C, Wang T, Quan J. Structural basis for the inhibition of Polo-like kinase 1. *Nat Struct Mol Biol*. 2013;20:1047.
62. Lowery DM, Lim D, Yaffe MB. Structure and function of Polo-like kinases. *Oncogene*. 2005;24:248–59.
63. Golan A, Yudkovsky Y, Hershko A. The cyclin-ubiquitin ligase activity of cyclosome/APC is jointly activated by protein kinases Cdk1-cyclin B and Plk. *J Biol Chem*. 2002;277:15552–7.
64. May KM, Reynolds N, Cullen CF, Yanagida M, Ohkura H. Polo boxes and Cut23 (Apc8) mediate an interaction between polo kinase and the anaphase-promoting complex for fission yeast mitosis. *J Cell Biol*. 2002;156:23–8.
65. Liu X, Zhou T, Kuriyama R, Erikson RL. Molecular interactions of Polo-like-kinase 1 with the mitotic kinesin-like protein CHO1/MKLP-1. *J Cell Sci*. 2004;117:3233–46.
66. Neef RD, Preisinger C, Sutcliffe J, Kopajtich R, Nigg EA, Mayer TU, et al. Phosphorylation of mitotic kinesin-like protein 2 by polo-like kinase 1 is required for cytokinesis. *J Cell Biol*. 2003;162:863–76.
67. Zhang Z, Hou SQ, He J, Gu T, Yin Y, Shen WH. PTEN regulates PLK1 and controls chromosomal stability during cell division. *Cell Cycle*. 2016;15:2476–85.
68. Tibarewal P, Zilidis G, Spinelli L, Schurch N, Maccario H, Gray A, et al. PTEN protein phosphatase activity correlates with control of gene expression and invasion, a tumor-suppressing phenotype, but not with AKT activity. *Sci Signal*. 2012;5:ra18.
69. Tamura M, Gu J, Matsumoto K, Aota S, Parsons R, Yamada KM. Inhibition of cell migration, spreading, and focal adhesions by tumor suppressor PTEN. *Science*. 1998;280:1614–7.
70. Gu T, Zhang Z, Wang J, Guo J, Shen WH, Yin Y. CREB is a novel nuclear target of PTEN phosphatase. *Cancer Res*. 2011;71:2821–5.
71. Zhang S, Huang WC, Li P, Guo H, Poh SB, Brady SW, et al. Combating trastuzumab resistance by targeting SRC, a common node downstream of multiple resistance pathways. *Nat Med*. 2011;17:461–9.
72. Shi Y, Wang J, Chandarlapaty S, Cross J, Thompson C, Rosen N, et al. PTEN is a protein tyrosine phosphatase for IRS1. *Nat Struct Mol Biol*. 2014;21:522–7.
73. Ben-David U, Amon A. Context is everything: aneuploidy in cancer. *Nat Rev Genet*. 2020;21:44–62.
74. Gordon DJ, Resio B, Pellman D. Causes and consequences of aneuploidy in cancer. *Nat Rev Genet*. 2012;13:189–203.
75. Sheltzer JM, Ko JH, Replogle JM, Habibe Burgos NC, Chung ES, Meehl CM, et al. Single-chromosome gains commonly function as tumor suppressors. *Cancer Cell*. 2017;31:240–55.
76. Wei W-J, Sun H-Y, Ting KY, Zhang L-H, Lee H-C, Li G-R, et al. Inhibition of cardiomyocytes differentiation of mouse embryonic stem cells by CD38/cADPR/Ca<sup>2+</sup>-signaling pathway. *J Biol Chem*. 2012;287:35599–611.
77. Wang Q, Guo W, Hao B, Shi X, Lu Y, Wong CW, et al. Mechanistic study of TRPM2-Ca<sup>2+</sup>-CAMK2-BECN1 signaling in oxidative stress-induced autophagy inhibition. *Autophagy*. 2016;12:1340–54.
78. Chin YR, Yuan X, Balk SP, Toker A. PTEN-deficient tumors depend on AKT2 for maintenance and survival. *Cancer discovery*. 2014;4:942–55.
79. Dunn KW, Kamocka MM, McDonald JH. A practical guide to evaluating colocalization in biological microscopy. *Am J Physiol-Cell Physiol*. 2011;300:C723–42.

## ACKNOWLEDGEMENTS

We thank members of Yue laboratory for advice on the manuscript. We would like to thank the Cryo-EM center of Southern University of Science and Technology for Cryo-EM data collection and the HPC-Service Station in Cryo-EM center of Southern University of Science and Technology for data processing.

## AUTHOR CONTRIBUTIONS

KZ, SL, HZ, and JY designed the experiments; KZ, YC, XS, ZM, HZ, ZY, RW and JY performed the experiments; KZ, YC, ZY, YG, CL, LZ, SL, HZ, and JY analyzed the data; and KZ, YC, HZ and JY wrote the paper.

## FUNDING

This work was supported by Hong Kong Research Grant Council grants (11101717 and 11103620 to JY), Ministry of Science and Technology of the People's Republic of China (2019YFA0906000 to HZ), NSFC (21778045, 32070702, and 82161128014 to JY), ITF (MRP/064/21 and GHP/097/20GD to JY), Guangdong Science and Technology Program (2017B030301018 to HZ), Shenzhen Science and Technology Innovation Committee (SGDX202011103093201010, JSGG20200225150702770, and JCYJ20210324134007020 to JY, and ZDSYS20140509142721429 to HZ).

**COMPETING INTERESTS**

The authors declare no competing interests.

**ETHICAL APPROVAL**

All animal experiments were performed following the university laboratory animal guidelines and with approval from the Animal Committee of City University of Hong Kong. Pathological sections of lung cancer patients were obtained from the Pathology Department of the Second Affiliated Hospital of Chongqing Medical University, with informed consent and approval from the Clinical Research Ethics Committee of the Second Affiliated Hospital of Chongqing Medical University. The patients were provided and signed the consent forms.

**ADDITIONAL INFORMATION**

**Supplementary information** The online version contains supplementary material available at <https://doi.org/10.1038/s41418-022-01000-4>.

**Correspondence** and requests for materials should be addressed to Shengjin Li, Hongmin Zhang or Jianbo Yue.

**Reprints and permission information** is available at <http://www.nature.com/reprints>

**Publisher's note** Springer Nature remains neutral with regard to jurisdictional claims in published maps and institutional affiliations.